International Journal of Concrete Structures and Materials

RESEARCH Open Access

Performance Optimization of Green Mortar Using Graded Ferrochrome Slag and Dune Sand as Aggregates

Hailong Wang[1,2], Junyi Shen[1], Qamar Shahzad[3], Xiaoyan Sun[1*] and Weiwei Dong[4]

Abstract

The massive expansion of global construction projects has caused a shortage of river sand (RS) as a construction raw material, necessitating the development of alternative materials to alleviate this pressure. In this study, ferrochrome slag (FS) and dune sand (DS) were utilized as composite aggregates to completely replace RS in building materials. Systematic tests were conducted to evaluate the effect of gradation on the flowability and mechanical properties of mortars with composite aggregates, clarifying the influence mechanism through microscopic physical phase tests. The test results show that the grading optimization improves flowability by 12.8–15.9% and enhances the 28-day compressive strength of mortars by 20.5–23.2%. The optimized gradation with a DS proportion of 0.3 has the highest performance, with 28-day compressive and flexural strengths of 59.81 MPa and 8.30 MPa, which are 29.4 and 11.9% higher than those of RS aggregate mortar, respectively. Microstructural analysis reveals that optimized gradation reduces porosity by 7.4–10%, leading to denser structures with fewer cracks and pores. The optimal use of DS and FS as alternative aggregates significantly reduces costs and potential carbon emissions, as the cost efficiency (C_p) and ECO_2 efficiency (CI) values of the optimized mixture decreased by 47.3 and 27.7% respectively, compared to the control group. The materials developed in this study exhibit excellent engineering application potential, and the performance-based material optimization method provides a theoretical basis and practical reference for the design of alternative building materials made with solid waste.

Keywords Dune sand, Ferrochrome slag, Grading optimization, Mechanical properties, Cost efficiency, Environmental impact

1 Introduction

With the accelerated development of global infrastructure and urbanization, the demand for sand for industrial and civil construction has increased significantly, leading to an increasingly prominent contradiction between supply and demand for river sand (RS) resources. Since 2014, the price of RS has continued to rise, and it is expected that in 2050 the price of RS will be twice as high as that in 2010 and the demand for RS will reach more than 2.5 times the supply (Gallagher & Peduzzi, 2019), as shown in Fig. 1. For safety and environmental considerations, the mining of RS has been restricted around the world in recent years, leading to a shortage of raw materials for concrete and a technical dilemma for the civil

Journal information: ISSN 1976-0485 / eISSN 2234-1315.

*Correspondence:
Xiaoyan Sun
selina@zju.edu.cn
[1] School of Civil Engineering and Architecture, Zhejiang University, Yuhangtang Road 866, Hangzhou 310058, Zhejiang, People's Republic of China
[2] Shanxi-Zheda Institute of New Materials and Chemical Engineering, Taiyuan 030006, China
[3] College of Civil Engineering, Tongji University, Shanghai 200092, China
[4] Centre for Balance Architecture, Zhejiang University, Hangzhou 310058, Zhejiang, China

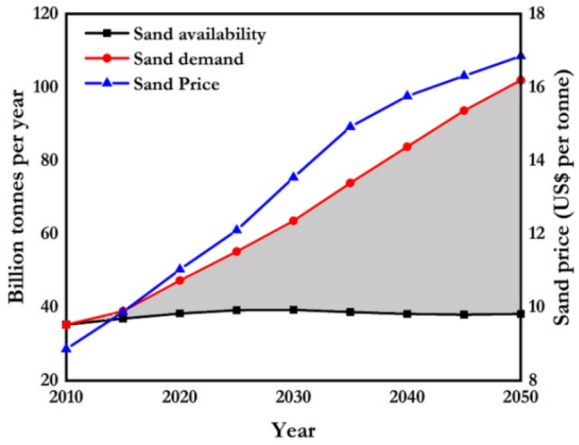

Fig. 1 Actual and forecast supply, demand and price curve of sand from 2010 to 2050 (Source: UNEP) (Gallagher & Peduzzi, 2019)

engineering industry (Dinh et al., 2022; Santhosh et al., 2021). Currently, various alternative aggregates have been explored, such as manufactured sand, sea sand, recycled sand, mine tailings, and waste glass. As summarized in Fig. 2, manufactured sand offers controllable quality and consistent gradation but suffers from high production costs and powder content (Attri et al., 2022; Jiang, 2022; Shi et al., 2021). Sea sand is abundant and low in silt but poses chloride-induced corrosion risks (Xiao et al., 2017). Recycled sand and mine tailings are eco-friendly and reduce waste, yet they face challenges of inconsistent quality and potential heavy metal contamination, respectively. Waste glass, while eco-friendly and possessing high hardness, carries risks of alkali-silica reaction and sharp edges. These limitations in cost, performance, and environmental impact highlight the urgent need to develop novel alternative aggregates to fully replace RS.

The application of dune sand (DS) for the construction industry is widely prospective due to its abundant reserves and ease of extraction (Abu Seif et al., 2016; Khattab, 2016). Meanwhile, with the rapid development of the ferrochrome alloy industry, global ferrochrome production now reaches 6.5–9.5 million tonnes annually (Koçyiğit, 2024; Nagarajan & Vijayan, 2023), with each metric tonne generating 1.0–1.6 tonnes of FS by-product, leading to an estimated annual FS production of 6.5–15.2 million tonnes, which occupies and destroys the land resources and pollutes the environment as solid waste. Available leaching tests validate that chromium immobilization in FS-based concrete complies with both China GB8978 (< 1.5 mg/L) for water leachability and the EU permanent waste requirements (< 0.5 mg/kg) for solid materials through matrix densification (Fares et al., 2021; Zhu et al., 2023), showing no detectable environmental risks. As shown in Fig. 3, since chromite and dunes are widely distributed globally and have significant spatial correlation effects (Alsharif et al., 2020; Team, 2007), it has become a development trend to manufacture low-carbon and environmentally friendly green building materials by utilizing dune sands and ferrochrome slag as alternative aggregates.

A summary of available literature on developing DS or FS as an alternative fine aggregate is provided in Fig. 4. Due to the low fineness modulus and smooth surface of DS, the compressive strength of mortars using dune sand

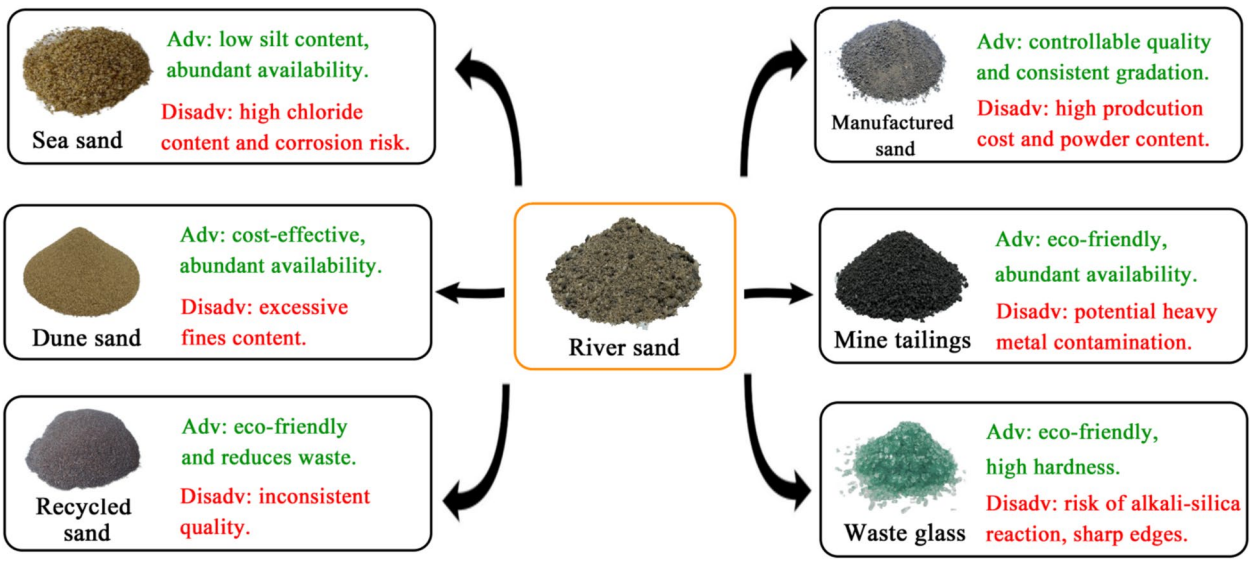

Fig. 2 Advantages and disadvantages of common alternatives to RS as aggregates

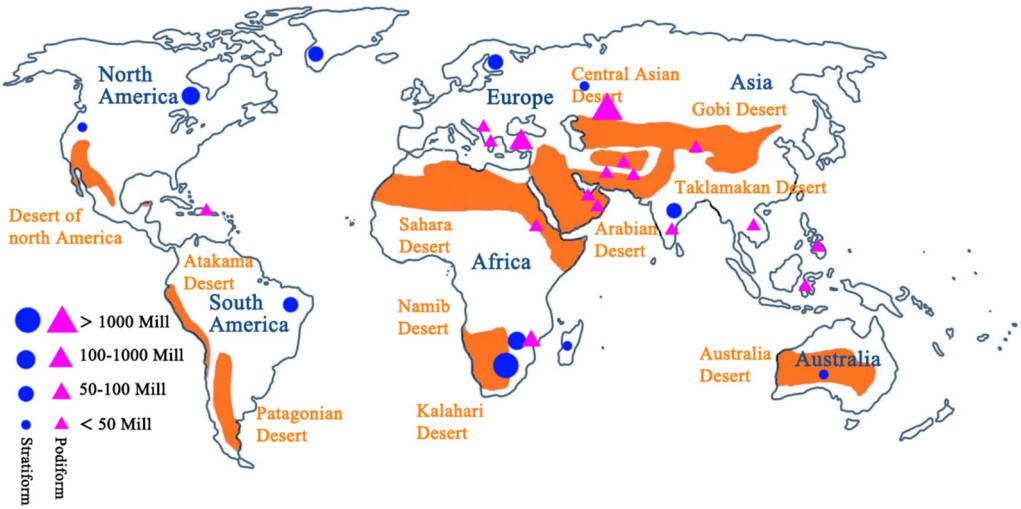

Fig. 3 Global chromite resources and dune distribution (Alsharif et al., 2020; Team, 2007)

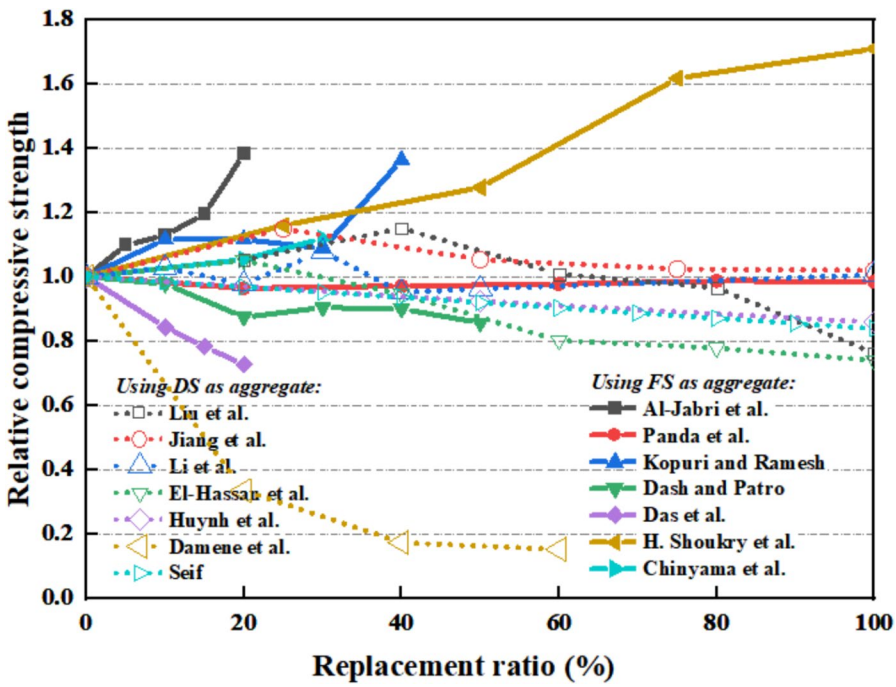

Fig. 4 Compressive strength of mortar with FS and DS as alternative aggregates (Al-Jabri et al., 2018; Chinyama et al., 2023; Damene et al., 2018; Das et al., 2021; Dash & Patro, 2018; El-Hassan et al., 2020; Huynh et al., 2022; Jiang et al., 2019; Kopuri & Ramesh, 2019; Li et al., 2020; Liu et al., 2020a, 2020b; Panda et al., 2013; Seif, 2013; Shoukry et al., 2022)

as aggregate is typically lower compared to RS (Damene et al., 2018; El-Hassan et al., 2020; Huynh, Ho, & Van Ho, 2022; J. Jiang et al., 2019; Y. Li et al., 2020; H. Liu et al., 2020a, 2020b; Seif, 2013). When DS substitution exceeds 20%, its high surface area and finer particles consume excessive cement paste, resulting in insufficient hydration products for particle encapsulation. This dilution effect triggers interfacial cracks and consequently drastic reductions in both workability and mechanical performance (El-Hassan et al., 2020). Although the very fine particles in desert sand may exert limited enhancement on the hydration process through heterogeneous nucleation and pozzolanic effects, they are insufficient to counteract the adverse impacts caused by physical deterioration. This

suggests that it is difficult for DS to realize a complete replacement of RS in mortar production. In contrast to DS, FS has a hard texture, porous appearance and rough surface. In terms of physical properties, the mechanical interlocking between FS particles and cement paste is enhanced compared to that of RS (Islam et al., 2021; Zelić, 2005). In terms of chemical properties, the formation of more calcium silicate hydrate (C-S-H) gels was promoted (Kumar et al., 2020; Ren et al., 2023). Therefore, the replacement of RS with FS as aggregate results in better mechanical properties of the mortar (Al-Jabri et al., 2018; Chinyama et al., 2023; Das et al., 2021; Dash & Patro, 2018; Kopuri & Ramesh, 2019; Panda, Mishra, Panda, Nayak, & Nayak, 2013; Shoukry et al., 2022). The compressive strength can be increased by 70.3% by replacing RS with some FS (Shoukry et al., 2022). However, due to the large particle size, irregular shape and poor grading of FS, the flowability of mortar tends to be lower at high substitution rates (Das et al., 2023; Dash & Patro, 2018), and the improvement of mechanical properties is not obvious or even decreased (Das et al., 2021; Dash & Patro, 2018; Panda et al., 2013). At present, only 30% of FS is developed and utilized as aggregate for road concrete (Sanghamitra & Reddy, 2017). Based on this, combining ultra-fine DS with porous FS may optimize gradation and improve workability. DS can fill the pores of FS, increasing packing density and enhancing mortar strength and durability.

Studies confirm that neither DS nor FS alone can fully substitute RS (Das et al., 2023; El-Hassan et al., 2020; Kopuri & Ramesh, 2019; Seif, 2013). Recent research, however, provides viable solutions through composite aggregate design. For instance, Manigandan and Ponmalar (2024) experimentally demonstrated that a 40% FS blend with crushed sand reduces the Ca/Si ratio to 1.0, promoting the elongation of silicate chains and the formation of denser calcium silicate hydrate (C-S-H) gels, which significantly enhances the compressive strength and compactness. This finding reveals the synergistic mechanisms of particle grading optimization and chemical activation in composite aggregates. Despite the progress made in the above studies, several critical challenges persist. First, existing research generally relies on empirical mixing ratios, lacking a scientific grading optimization method based on the theory of particle densification, which limits the performance improvement of composite aggregates. Second, the physical filling effects and chemical interaction mechanisms when DS and FS are combined remain unclear, which hinders the full expression of their synergistic effects. Finally, current research mainly focuses on partial substitution, with insufficient studies on fully replacing natural sand and a lack of multi-objective evaluation systems.

In this study, an innovative approach is proposed to achieve complete replacement of RS in mortar production by developing a composite aggregate system comprising DS and FS. The novelty of this research includes optimizing the particle size distribution of the composite aggregate using the maximum packing theory, which results in enhanced microstructural densification and improved interfacial integrity compared to conventional gradation methods; investigating the action mechanism and influencing factors of mortar performance through relevant experiments, and establishing a design method for composite aggregates to fully replace RS; and establishing a multi-index evaluation framework that encompasses compressive strength, flowability, and interfacial bonding strength, integrated with cost–benefit ratio and embodied CO_2 (ECO_2) emission efficiency indices, to achieve a quantitative synergy of performance, economic, and environmental benefits. This strategy offers a sustainable solution to reduce RS dependence and provides guidance for using industrial solid waste in green building materials.

2 Materials and Experimental Program

2.1 Materials

The mortar cement used was sulphoaluminate cement (42.5 SAC) produced by Wuxi Golden Eagle Building Materials Company, Jiangsu Province, China, with a specific surface area of 449m^2/kg and a specific gravity of 2.95 g/cm^3. RS was taken from Fuchun River, Zhejiang Province, China. DS was taken from Kubuqi Desert, Inner Mongolia, China. FS was supplied by Minto Group, Baotou City, Inner Mongolia.

The physical properties of the three materials were determined according to the measurement methods of ASTM C29, ASTM C33, ASTM C128 and GBT 14684-2011 ("ASTM C29: Standard Test Method for Bulk Density ("Unit Weight") and Voids in Aggregate," 2017; "ASTM C33: Standard Specification for Concrete Aggregates," 2019; "ASTM C128: Standard Test Method for Relative Density (Specific Gravity) and Absorption of Fine Aggregate," 2015; "GB/T 14684–2011: Sand for Construction(in Chinese)," 2011), as shown in Table 1. The fineness modulus and water absorption of DS were 40 and 16% of those of RS, respectively. The fineness modulus and water absorption of FS were 152 and 72% of those of RS, respectively.

X-ray diffraction (XRD) analysis was performed using a Bruker D8 Advance diffractometer (Germany) with Cu Kα radiation (λ = 1.5406 Å) operated at 40 kV and 40 mA. Sample preparation strictly followed the ASTM E1915 standard: raw materials were crushed and sieved through a 325-mesh (45 μm) sieve, and approximately 1.0 g of the sieved powder was loaded into the sample

Table 1 Physical properties of DS, RS, and FS

Materials	Apparent density (kg/m^3)	Specific density (kg/m^3)	Fineness modulus	Water Absorption (%)	Silt contents (%)
RS	1433	2504	2.625	3.64	1.56
DS	1632	2627	1.053	0.60	0.50
FS	1436	2910	3.982	2.61	0.91

The parameters with apparent density were determined by ASTM C29, specific gravity and water absorption capacity of aggregates were determined by ASTM C128, silt content was determined by ASTM C33, and fineness modulus was determined by GBT 14684–2011

holder. All samples were oven-dried at 105 °C for 24 h prior to testing to eliminate moisture effects. Scans were conducted from 10° to 90° (2θ) with a step size of 0.02° and a scanning rate of 0.02°/s. Phase identification was achieved using Jade 9.0 software integrated with the ICDD-PDF4 + database. X-ray fluorescence (XRF) analysis followed identical sample preparation procedures and was carried out using a Bruker S8 TIGER spectrometer for elemental determination. The phase compositions and chemical compositions of the above materials were determined using X-ray diffraction analysis (XRD) and X-ray fluorescence analysis (XRF) as shown in Fig. 5 and Table 2. The XRD results indicate that DS and RS exhibit typical characteristics of quartz crystal structure, with high-intensity, concentrated diffraction peaks, suggesting good crystallinity and a relatively uniform structure. In contrast, the phase composition of FS includes not only silica but also some amorphous materials and multiple other phases, such as magnesium chromite and forsterite. The diffraction peaks of FS are relatively broader and less intense, with a more dispersed peak distribution, reflecting lower crystallinity and a more complex structure. This structural difference is closely related to the rapid cooling process during its air-cooled formation. In terms of chemical composition, both DS and RS are siliceous with about 90% SiO_2 content. The content of SiO_2 in FS is only 34.8%, and the content of CaO and MgO in FS is relatively high, with a certain amount of Cr_2O_3. Figures 6 and 7 show the macroscopic stacking state images and scanning electron microscope (SEM) images of the three aggregates, respectively. It can be seen that the particles of DS and RS have similar hemispherical shapes and smooth textures. In contrast, the morphology of the FS particles has special characteristics with sharp edges and rough texture.

The compactness and flowability of mortar are greatly influenced by particle size and aggregate morphology (Behera et al., 2019; Güneyisi et al., 2015). In order to further analyse the morphology and characteristics of aggregates, 100 particle samples were randomly selected from each aggregate and clear magnified images were obtained with a digital camera. The boundaries of each particle image were separated and summarized by graphic processing software ImageJ, as shown in Fig. 8. According to ISO 9276-6, in order to analyse the elongation, closeness to roundness and concavity of the aggregate particles, the

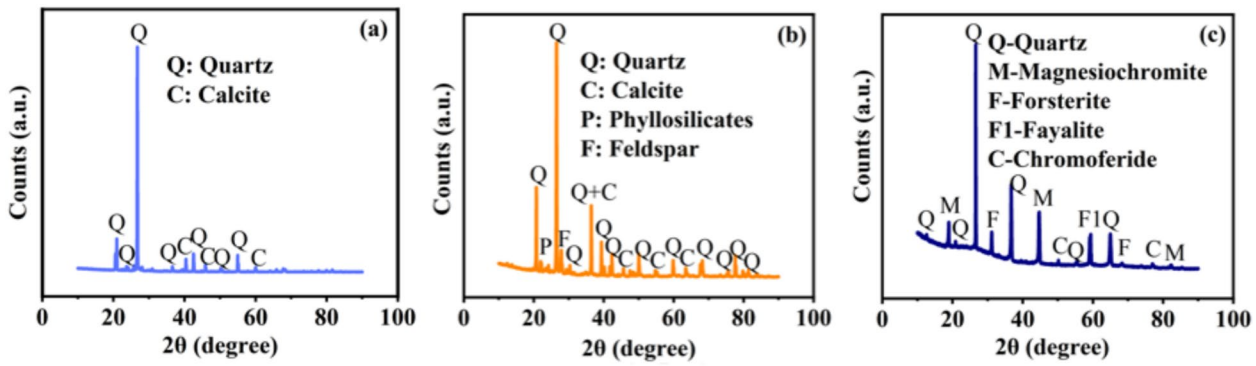

Fig. 5 XRD patterns of the materials used: **a** RS, **b** DS, and **c** FS

Table 2 Chemical composition of the materials used (wt.%)

Contents	SiO_2	Al_2O_3	Fe_2O_3	CaO	MgO	Na_2O	K_2O	TiO_2	ZrO_2	Cr_2O_3	SO_3	LOI
RS	90.5	2.40	1.4	0.5	0.4	0.3	0.5	0.1	–	–	0.1	3.9
DS	88.4	2.7	0.9	1.4	0.5	0.3	0.3	0.2	0.2	–	–	5.1
FS	34.8	24.6	4.1	5.1	18.1	0.5	0.4	0.7	–	5.7	1.1	5.0

LOI means Loss on ignition

Fig. 6 General aspects of the materials used: **a** RS, **b** DS and **c** FS

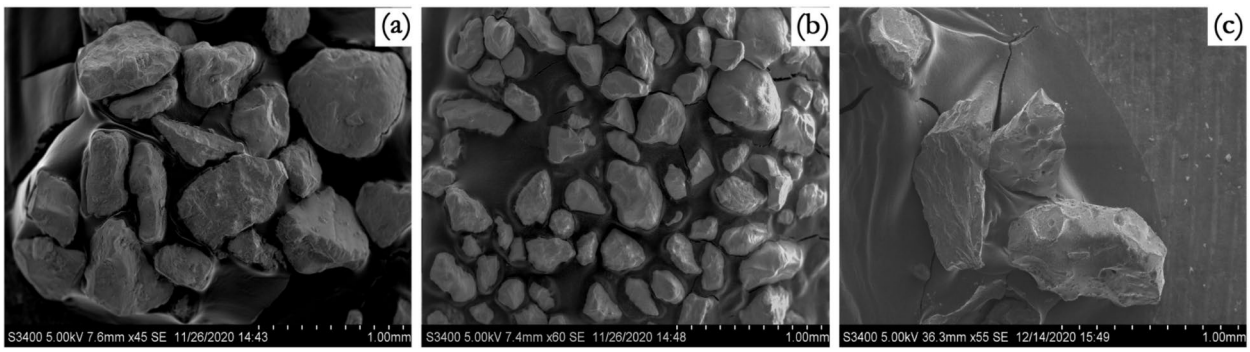

Fig. 7 SEM images of the materials used (a general aspect of the grains): **a** RS, **b** DS, and **c** FS

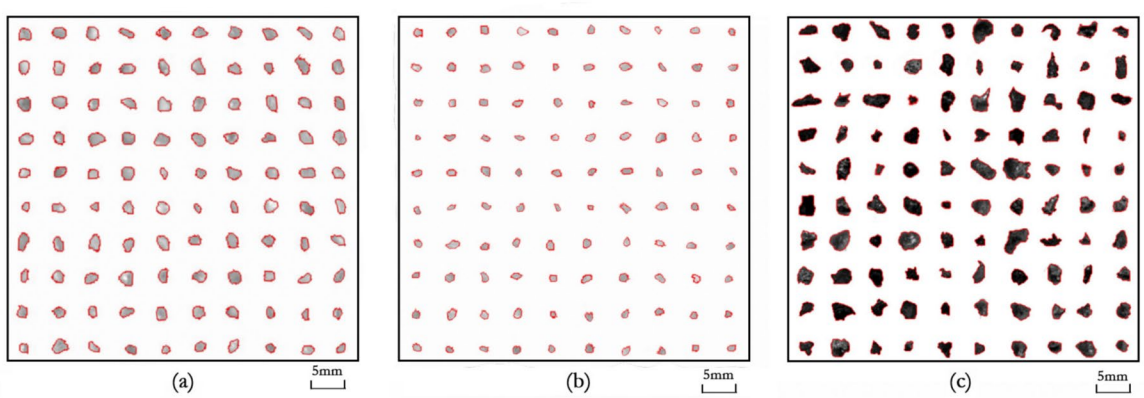

Fig. 8 Magnified images of the aggregate particles: **a** RS, **b** DS, and **c** FS

aspect ratio (A_r), circularity (C_i) and convexity (C_o) were chosen as the particle shape parameters, which can be obtained by the following equations:

$$A_r = \frac{X_{Fmin}}{X_{Fmax}} \tag{1}$$

$$C_i = \sqrt{\frac{4\pi A}{P^2}}, and \tag{2}$$

$$C_o = \frac{P_c}{P} \tag{3}$$

where A is the area of the particle projection, P is the perimeter of the particle projection, P_c is the perimeter of the convex hull around the particle, and x_{Fmax} and x_{Fmin} are the maximum and minimum Feret diameters of the

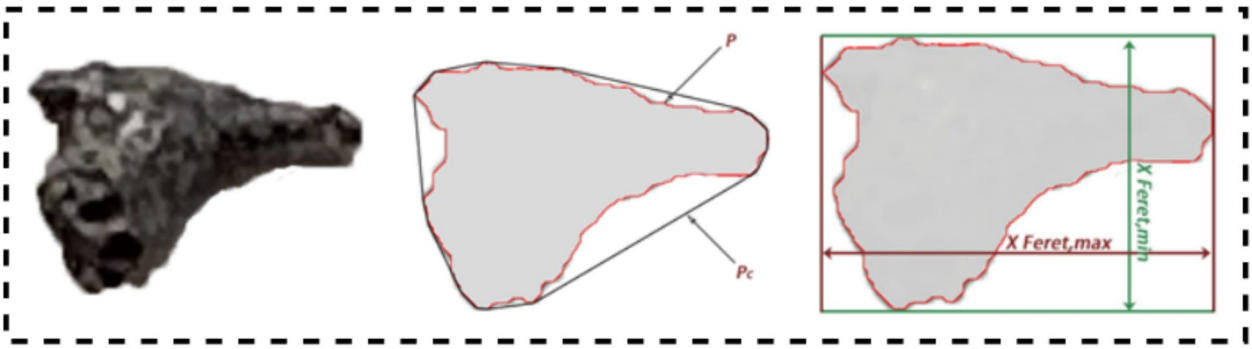

Fig. 9 Shape parameters of an FS particle for morphology characterization

Table 3 Shape parameters of the aggregates

Aggregate category	Aspect ratio (A_r)	Circularity (C_i)	Convexity (C_o)
RS	0.85	0.88	0.98
DS	0.86	0.90	0.98
FS	0.72	0.77	0.94

particle. In the case of FS, the particle shape parameters used for morphological characterization are shown in Fig. 9.

Due to long-term weathering and erosion or water scouring, DS and RS show smooth and variable shapes. FS, in contrast, usually has an angular shape due to processes such as melting, selection and crushing. The results of the shape parameters obtained by processing the aggregate particle images using computer analysis are presented in Table 3. Analysis of the data shows that of the three aggregates, DS has the highest roundness and RS has a moderate roundness. FS has the lowest roundness, indicating a more irregular shape or rougher surface. The rougher surface of FS provides a larger contact area with the attached cement paste, thereby improving adhesion (Elibol & Sengul, 2016). However, the irregular shape of FS can impede optimal particle packing due to increased void content and interparticle friction, leading to an adverse effect on fresh behaviour in slump, compaction factor, and Vee-Bee tests of the prepared mortar (Das et al., 2023; Dash & Patro, 2018; Manigandan & Ponmalar, 2022). Therefore, the simultaneous use of DS aggregates with high roundness and smoothness and FS aggregates with low roundness and smoothness is an important technical requirement to improve aggregate packing compactness and mortar workability and mechanical properties.

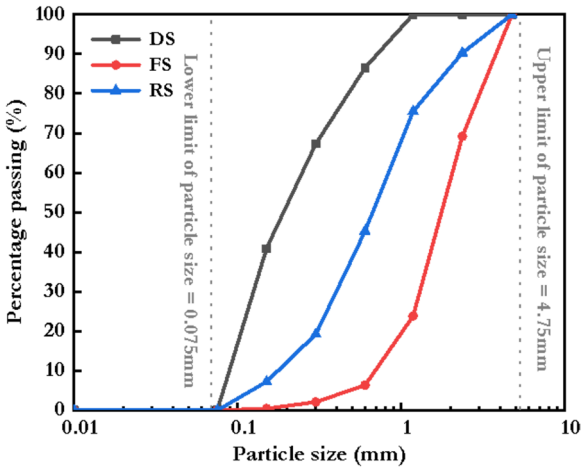

Fig. 10 Particle size distribution curves for DS, FS, and RS

2.2 Composite Aggregate Design Based on Grading Optimization

Considering the adverse effects of very fine particles on the performance of concrete or mortar (Achour et al., 2019), particles with a diameter of less than 0.075 mm were removed in advance. Screening analysis was used to obtain a particle size distribution curve for the aggregates according to ASTM C33 ("ASTM C33: Standard Specification for Concrete Aggregates," 2019), which is shown in Fig. 10. There is a significant difference in the particle size distribution between the two aggregates. The particle size of DS is predominantly distributed between 0.075 mm and 0.30 mm, while the particle size of FS is predominantly distributed between 0.60 mm and 2.36 mm. The composite aggregate system lacks medium-sized particles, leading to discontinuous grading. This increases void content and reduces FS interlocking, causing FS particle settlement and DS or paste flotation, ultimately resulting in mortar segregation and impairing strength and durability. (H. Li et al., 2021; Luo et al., 2022).

A portion of the DS smaller than 0.30 mm particle size range was screened to prevent the fine particles from adversely affecting the workability and bonding strength of the mortar (Zhang et al., 2022). In addition, particles in the medium particle size range are added to improve the roundness of roughly shaped, irregular and angular FS aggregates. FS in the particle size range between 0.30 mm and 1.18 mm was added by mechanical milling method as shown in Fig. 11. A comparative analysis of aspect ratio, roundness and convexity of 100 randomly sampled FS particles before and after ball milling was carried out and is shown in Fig. 12. The ball milled FS particles can be approximated as spheres.

Subsequently, the particle gradation was optimized based on the theory of compact packing proposed by Dinger and Funk (Dinger & Funk, 1997). The Dinger-Funk equation can be expressed as:

$$P(D) = \frac{D^n - D_{min}^n}{D_{max}^n - D_{min}^n} \tag{4}$$

where *P(D)* is the proportion of particles smaller than the particle size *D*, D_{max} and D_{min} are the maximum and minimum particle sizes, respectively, and *n* is the distribution parameter. For fine aggregate systems, *n* is usually set between 0.2 and 0.4 (Cui, Liu, Yao, & Lin, 2010; Peng et al., 2020).

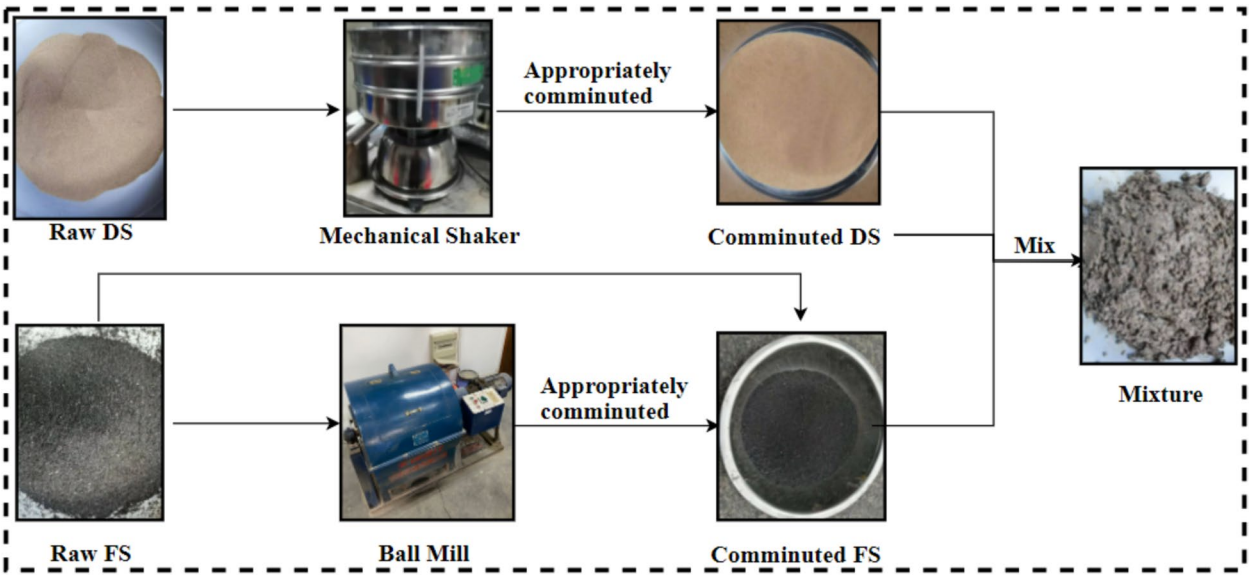

Fig. 11 Mixing procedure of the samples

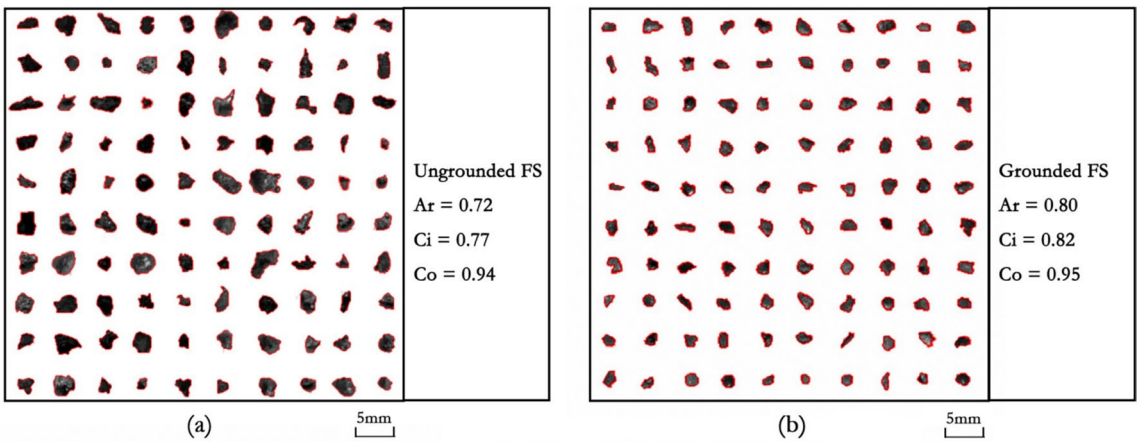

Fig. 12 Magnified images and shape parameters of the aggregate particles. **a** before ball milling **b** after ball milling

In order to study the optimal combination ratio of FS and DS, *n was* set to be 0.2, 0.3 and 0.4, respectively, and 1×6 vectors were used to represent the percentage of particles in different particle sizes of each aggregate in the ranges of 0.075–0.15 mm, 0.15–0.30 mm, 0.30–0.60 mm, 0.60–1.18 mm, 1.18–2.36 mm and 2.36–4.75 mm. V_{DS}, V_{FS} and $V_{D\text{-}F}$ represent the vectors extracted from the measured gradation curves of DS and FS aggregates and the theoretical curves calculated based on the Dinger-Funk equation, respectively. *Xi*, *Yi* and *Ai* are the elements in the above vectors, $i = 1, 2, \ldots 6$.

$$V_{DS} = [X_1 X_2 X_3 X_4 X_5 X_6]^T \tag{5}$$

$$V_{FS} = [Y_1 Y_2 Y_3 Y_4 Y_5 Y_6]^T \tag{6}$$

$$V_{D-F} = [A_1 A_2 A_3 A_4 A_5 A_6]^T \tag{7}$$

By optimizing the percentage of aggregate particle size to make the aggregate blend close to the tightest fit curve, when sieving out the DS of particle size 0.075–0.30 mm, and adding the FS of particle size 0.30–1.18 mm range, the following equations can be obtained:

$$V'_{DS} = \left[X'_1 X'_2 X'_3 X'_4 X'_5 X'_6\right]^T \tag{8}$$

$$V'_{FS} = \left[Y'_1 Y'_2 Y'_3 Y'_4 Y'_5 Y'_6\right]^T \tag{9}$$

The following relationship exists between the vectors V_{DS} and V'_{DS}:

$$\frac{X'_3}{X_3} = \frac{X'_4}{X_4} = \frac{X'_5}{X_5} = \frac{X'_6}{X_6} \tag{10}$$

Similarly, the following relationship exists between the vectors V_{FS} and V'_{FS}:

$$\frac{Y'_1}{Y_1} = \frac{Y'_2}{Y_2} = \frac{Y'_5}{Y_5} = \frac{Y'_6}{Y_6} \tag{11}$$

Let α be the proportion of DS in the mass of the combined aggregate, $\alpha = \frac{MassofDS}{Totalmassofaggregate}$, and characterize the extreme values of the residual sum of squares (*RSS*) of the Dinger-Funk theoretical curves in terms of the curves after optimization of gradation as follows:

$$RSS = \sum_{i=1}^{6} \left[\alpha \times X'_i + (1-\alpha) \times Y'_i - A_i\right]^2 \tag{12}$$

The minimize function in the Python SciPy library was called to optimize this set of values using the optimization algorithm. The results show that when the distribution modulus *n* is 0.4, 0.3, and 0.2, the *RSS* extremes correspond to α of 0.314, 0.392, and 0.489, respectively, and thus α is taken to be 0.3, 0.4, and 0.5 in the aggregate combination design.

Based on the three combination ratios, a total of seven different mortar ratios were set for direct combination aggregates (D-0.3, D-0.4 and D-0.5), gradation-optimized combination aggregates (O-0.3, O-0.4 and O-0.5) with RS control group R0, as shown in Table 4.

Figure 13 shows the gradation curves of the two aggregates after a direct combination of mixing and grade optimization combination, and it can be seen that the curves of gradation D-0.3, D-0.4, and D-0.5 for the direct combination of aggregates are outside of the particle grading boundaries specified in ASTM C33 ("ASTM C33: Standard Specification for Concrete Aggregates," 2019); whereas the gradation curves of grade optimization, O-0.3, O-0.4, and O-0.5 are within the boundaries.

2.3 Experimental Procedures

The corresponding mass of raw materials was weighed according to the mixing ratios in Table 4. First, a small mortar mixer was used to dry mix for 2 min until the mixture was homogeneous. Then, water was slowly added to the mixture for 20 s. Finally, wet mixing was carried out for 120 s to obtain the test mortar. The flow of the fresh mortar mixture was tested and specimens were made to test the compressive strength, flexural strength,

Table 4 Mixing proportion of mortar (kg/m^3)

Mix ID			Cement	Water	DS	FS	RS
Reference mixes	R0		490	245	–	–	1470
Direct mixes	D-0.3	α = 0.3			735	735	–
	D-0.4	α = 0.4			558	882	–
	D-0.5	α = 0.5			441	1029	–
Optimized mixes	O-0.3	α = 0.3			735	735	–
	O-0.4	α = 0.4			558	882	–
	O-0.5	α = 0.5			441	1029	–

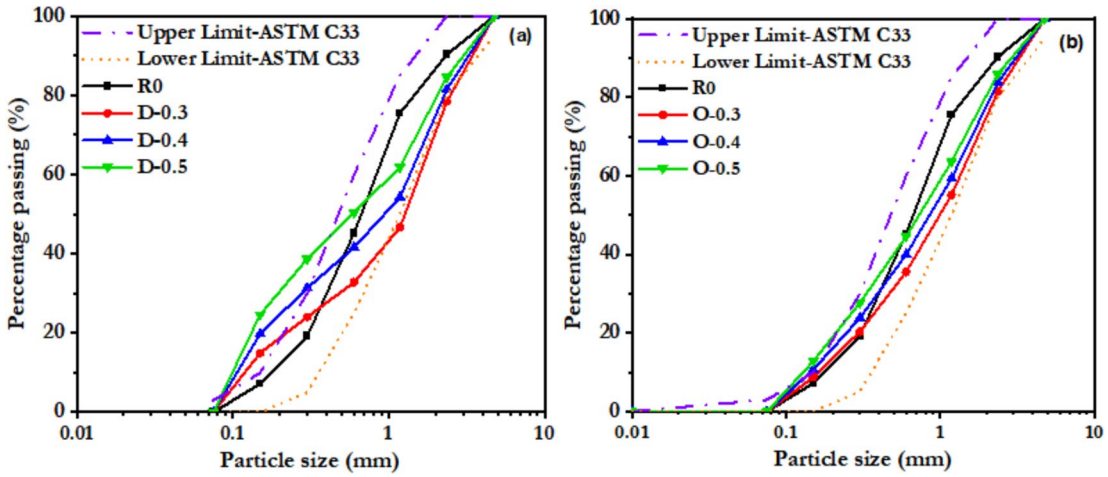

Fig. 13 Particle size distribution curves: **a** non-optimized mix and **b** optimised mix

split tensile strength and modulus of elasticity. All specimens were demolded after 24 h of pouring and then cured in water at 25 ± 2 °C until the test age was reached. The tests were repeated three times at each age for each set of ratios and the average values were taken. Samples were also prepared for microstructure testing.

The flowability of the mixes was measured according to the ASTM C1437 ("ASTM C1437-15: Standard Test Method for Flow of Hydraulic Cement Mortar," 2015) standard test method using an FT-E01 flow meter manufactured by Hebei Cangzhou Instrument and Equipment Company Limited, China. The desired mortar material was first filled into a mould, which was placed on a hopping table and left to stand for 1 min, then the excess mix was gently smoothed out using a spatula, the mould was removed, and then vibrated 25 times on an automatic hopping table. The diameter of the material was measured along six evenly distributed directions, and the average value was taken as the flowability result.

The compressive strength was measured according to the standard test method of JGJ70-2009 ("JGJ70-2009: Standard for test method of performance on building mortar.," 2009), using a YEP-1000 semi-automatic compression testing machine produced by China Shanghai Hualong Testing Instrument Co. Cubic specimens with dimensions of 70.7 × 70.7 × 70.7 mm^3 were prepared and measured after 1, 3, 7, and 28 d of curing at a constant loading rate of 0.5 MPa/s.

Flexural strength tests were carried out using a 25 t Instron universal testing machine according to the ASTM C348 standard test method ("ASTM C348: Standard test method for flexural strength of hydraulic-cement mortars," 2019). Prismatic test blocks of size 40 × 40 × 160 mm^3 were prepared and the tests were carried out after 1, 3, 7 and 28 d of curing. The tests were carried out using the three-point loading method with a constant loading rate of 0.5 MPa/s.

Split tensile strength tests were conducted according to the ASTM C496 standard method ("ASTM C496: Standard Test Method for Splitting Tensile Strength of Cylindrical Concrete Specimens," 2017) using the same loading apparatus as for compressive strength tests. Cylindrical mortar specimens with a diameter of 150 mm and a height of 300 mm were prepared and the tests were carried out after 3, 7, 14 and 28 d of curing at a constant loading rate of 0.5 MPa/s, and the split tensile strength was calculated by destructive loading.

The modulus of elasticity was measured using prismatic specimens with dimensions of 70.7 × 70.7 × 200 mm^3 at 28 days according to the JGJ 70-2009 standard test method ("JGJ70-2009: Standard for test method of performance on building mortar.," 2009). During the testing process, a preloading test was first performed, where 40% of the measured compressive strength of the previously prepared specimens of the same size was used as the initial load, applied at a rate of 0.5 MPa/s. The load was then slowly unloaded, repeated twice, and then formally loaded up to the maximum load, which was one-third of the compressive strength of prismatic specimens of the same size. Stress and strain were measured during this process using a strain gauge and the modulus of elasticity was calculated.

The microstructure was analysed using a JSM-5900 scanning electron microscope manufactured by JEOL, Japan, to test the microstructure. The samples obtained from the compressive strength test at the age of 28 days were selected and dried in an oven below 40 °C. Subsequently, SEM tests were carried out and the porosity was determined by identifying the images obtained from the SEM using ImageJ software.

A comprehensive cost analysis and ECO_2 emission index calculation were conducted for all test sequences to evaluate their economic efficiency and environmental (or green) impact. The ECO_2 emission analysis is broadly divided into three stages: the material stage, the transportation stage, and the production stage. In this study, the ECO_2 emissions from the transportation and production stages were negligible in comparison to the material production stage, and thus were not considered. The relevant material costs and ECO_2 emission data, as shown in Table 5, were obtained from suppliers and other literature (M. Liu et al., 2023; Mishra et al., 2022; Shang, Wu, Lu, Yao, & Wang, 2022; Zhang et al., 2022), with the production cost of FS assumed to be zero (Moyo et al., 2022).

To quantitatively characterize the cost and environmental benefits of the prepared mortar, the cost efficiency per cubic meter of mortar *Cp* (USD/m^3·MPa) and the ECO_2 efficiency *CI* (kg/MPa·m^3) were calculated using the following expressions (C. Ma et al., 2020), based on its 28-day compressive strength.

Table 5 Details of the used materials

Materials	Cost (USD/ton)	ECO_2 (kg CO_2/ton)
Cement (42.5 SAC)	145.76 (From the supplier)	608.4 Shang et al., (2022)
Water	0.46 Zhang et al., (2022)	1.0 Zhang et al., (2022)
DS	6.18 Zhang et al., (2022)	0.148 Liu et al., (2023)
FS	0.59 Mithun et al., (2016)	0 Yaragal et al., (2020)
RS	27.05 Zhang et al., (2022)	13.9 Zhang et al., (2022)

$$C_p = \frac{\sum Cost}{f_c} \tag{13}$$

$$CI = \frac{\sum ECO_2}{f_c} \tag{14}$$

where f_c is the 28-day compressive strength (MPa) of the mortar, $\sum Cost$ and $\sum ECO_2$ are the total cost (USD/m^3) and total potential carbon emission (kg/m^3) of the materials used in 1 cubic meter of mortar, respectively.

To investigate the influence of composite aggregate proportions on mortar performance and the intrinsic relationships among various performance indicators, Pearson correlation coefficients were employed for statistical analysis. This method quantifies the correlations between variables such as flowability, compressive strength, flexural strength, split tensile strength, and porosity. The Pearson correlation coefficient assumes that the variables follow a Gaussian distribution, with values ranging from −1 to 1, −1 indicates a complete negative linear correlation, 0 indicates no linear relationship, and +1 indicates a complete positive linear correlation. The calculation formula is shown in Eq. (15):

$$r = \frac{\sum_{i=1}^{n}(x_i - \overline{x})(y_i - \overline{y})}{\sqrt{\sum_{i=1}^{n}(x_i - \overline{x})^2 \sum_{i=1}^{n}(y_i - \overline{y})^2}} \tag{15}$$

where r is the Pearson correlation coefficient, x_i and $\overline{x}$ are the observed values and mean of variable x, respectively, and y_i and $\overline{y}$ are the observed values and mean of variable y, respectively.

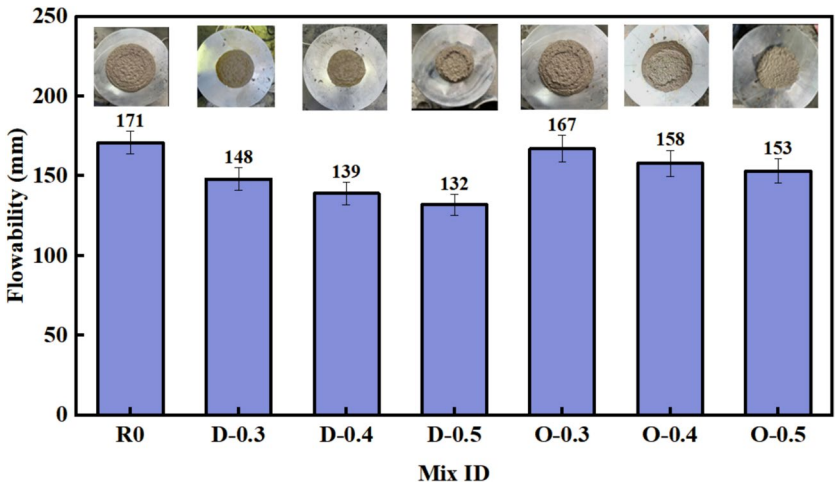

Fig. 14 Flowability of the mortar at different mix ratios

3 Flowability and Mechanical Properties

3.1 Flowability

Flow tests were conducted on all fresh mixes and the results are shown in Fig. 14. The reference mix R0 exhibited the highest flowability, reaching 171 mm, which was 2.4–29.5% higher compared to the composite aggregate mixes. This difference was attributed to the increased specific surface area due to the fine grain size of the dune sand, as well as the lower sphericity and circularity of the combined aggregates, which increased the frictional resistance (Das et al., 2023; Dash & Patro, 2018; Zhang et al., 2022).

In the test group using composite aggregates, the change in flowability was related to the mass share factor α of DS in the composite aggregate, which was 148 mm, 139 mm, and 132 mm for sequences D-0.3, D-0.4, and D-0.5, respectively. D-0.3 exhibited the highest level of flowability among the new composite aggregate sequences, and as α increased from 0.3 to 0.5, the flowability decreased by 10.8%. When the DS substitution rate is too high, the excess DS consumes a large amount of paste, which makes the paste encapsulated on the aggregate surface thinner and the lubricating effect of the paste on the aggregate is weakened, leading to a reduction in the flowability of the mix (El-Hassan et al., 2020; Liu et al., 2020a, 2020b; Zhang et al., 2022).

After grading optimization, the flow of test sequences O-0.3, O-0.4 and O-0.5 were 167 mm, 158 mm and 153 mm, respectively, with O-0.3 exhibiting the highest flow among all composite aggregate sequences. When α increased from 0.3 to 0.5, the flowability decreased by 8.4%. After grading optimization, the flowability of the composite aggregate mixes improved by 12.8–15.9%. The improved aggregate grading caused an increase in the flowability of the mixes, possibly due to the fact that gradation optimization reduces the pore space between the particles in the mixes, which reduces the resistance of the particles to flow and makes the mixes easier to flow (Khan et al., 2016; Zhang et al., 2019a, 2019b).

The morphological parameters of aggregates positively or negatively affect the flowability of the mixes. A multi-parameter linear regression analysis was used to quantitatively characterize the effects of different aggregate morphological parameters on the flowability of fresh materials. Four parameters including aspect ratio, circularity, convexity and fineness modulus were selected as morphological parameters in the statistical analysis. The multi-parameter model for the flowability of fresh mixes and the morphological parameters of aggregates is as follows:

$$F = 396.9 \times A_r + 245.7 \times C_i + 39.6 \times C_o + 60.0 \times F_m - 577.4 \quad (16)$$

where F is the flowability of the fresh mix, and A_r, C_i, C_o, and F_m are the aspect ratio, circularity, convexity, and fineness modulus of the aggregate, respectively.

The input parameters of aggregate morphology and the predicted results of each experimental sequence are summarized in Table 6, where the data in brackets within the

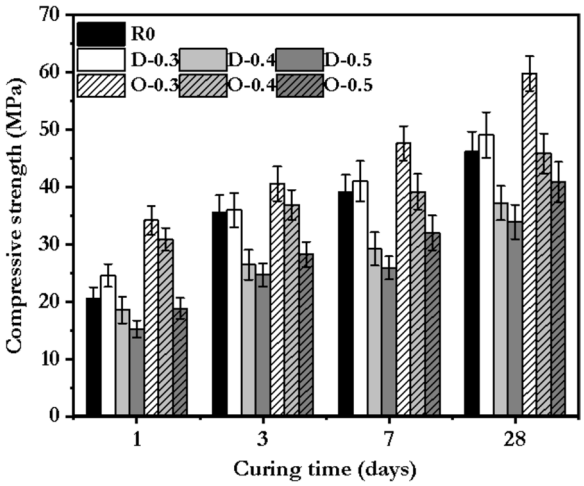

Fig. 15 Compressive strength of the mortar with different aggregates

Table 6 Summary table of aggregate morphology parameters and fresh mixes flowability regression results

Mix ID	Aspect ratio (A_r)	Circularity (C_i)	Convexity (C_o)	Fineness modulus (F_m)	Predicted values (mm)
R-1.0	0.85	0.88	0.98	2.625	172 (+1)
D-0.3	0.76	0.81	0.95	3.103	147 (−1)
O-0.3	0.78	0.82	0.95	3.311	169 (+2)
D-0.4	0.78	0.82	0.96	2.810	139 (0)
O-0.4	0.79	0.83	0.96	3.035	160 (+2)
D-0.5	0.79	0.84	0.96	2.518	130 (- 2)
O-0.5	0.80	0.84	0.96	2.738	150 (−3)

predicted values indicate their error from the test results. In Table 6, the error range between the predicted values and the experimental values is from -3 mm to +2 mm, with an error rate of less than 2.7%. The contribution of morphological parameters to the flowability from large to small is as follows: aspect ratio (53.5%), circularity (33.1%), fineness modulus (8.1%), and convexity (5.3%).

3.2 Compressive Strength

The compressive strength of each mortar test sequence was tested at 1, 3, 7 and 28 days as shown in Fig. 15. The strength of control R0 at 1, 3, 7, and 28 days was 20.54, 35.65, 39.17, and 46.2 MPa, respectively. When no grading optimization was taken, the test sequence D-0.3 still showed better compressive strength than the control at all ages, 16.6, 1.0, 4.6, and 5.9% higher than R0 at 1, 3, 7, and 28 days, respectively, which suggests that the novel composite aggregate can replace RS in appropriate proportions and be used as a better building material. The reasons for this are as follows: DS fills most of the gap between the aggregate and the paste (Jiang et al., 2019; Zhang et al., 2019a, 2019b), and it facilitates the action of the catalytic multiphase nucleation process to form additional calcium silicate hydrate embedded in the cement paste (Zhang et al., 2022). Under this dual physical and chemical filling effect, the mortar structure is significantly denser.

Tests show that the composite ratio α significantly affects the compressive strength, α from 0.3 to 0.5 can lead to a reduction of compressive strength by 32.2% at 28 days, and even show worse mechanical properties than the control group R0. The compressive strength value of D-0.5 is lower than that of the R0 group by 19.3–26.5% at all ages, and the decrease in strength may be due to the increase in the number of fine-sized DS leading to a gradual increase in specific surface area. The gradual increase in the specific surface area due to the increase in the number of fine DS particles makes it difficult for the mortar to completely cover the aggregates and achieve full hydration (Kaufmann, 2020; Li et al., 2020; Liu et al., 2020a, 2020b); secondly, the decrease in the percentage of FS aggregates results in a lower hydration reaction induced by the amorphous glass phase oxide that they contain; and lastly, the increase in the number of DS particles with smooth surfaces is accompanied by a decrease in the percentage of rough FS particles (Das et al., 2023; Xia et al., 2023), which decreases the adhesive strength between the aggregates and the cement paste.

Figure 15 shows that grading optimization improves the compressive strength of composite aggregates, with 20.5–23.2% strength improvement at 28 days of age at different composite ratios. O-0.3 exhibits the maximum compressive strength at all ages, and although its early strength improvement is not significant, the compressive strength is significantly increased at 28 days of age, which is 29.4% higher than R0. The increase in compressive strength due to grading optimization is attributed to the reduction of the internal porosity of the mortar (De Larrard & Sedran, 1994; Sevim & Demir, 2019). However, the compressive strengths of O-0.4 and O-0.5 were lower than R0 by about 7.5% and 17.1%, respectively, suggesting that the optimized gradation aggregates are still not suitable for higher combination ratios α.

3.3 Flexural Strength

Flexural strength was tested at 1, 3, 7 and 28 days for all test sequences and the results are shown in Fig. 16. The flexural strength of control R0 at different ages ranged from 4.43 to 7.42 MPa. The direct-mixed composite aggregate mortar test sequence exhibited worse flexural strength than the control at all ages and decreased with increasing α. The flexural strengths of D-0.3, D-0.4, and D-0.5 were 6.25, 5.95, and 5.75 MPa, respectively, at 28 days, which were 15.8, 19.8, and 22.5% lower than that of R0, indicating that the new composite aggregates without grading optimization could not replace RS in the index of flexural strength. When α was raised from 0.3 to 0.5, the flexural strength of the samples decreased by 8.0%. The effect of aggregate composite ratio α on flexural strength is lower than that on compressive strength, which may be due to the fact that FS with rough surface accounts for a larger portion of the aggregate, resulting in a better bond between aggregate and paste, and hence relatively higher deformability of the composite aggregate mortar.

Figure 16 shows that the 28-day flexural strength of the test sequence with optimized gradation at different

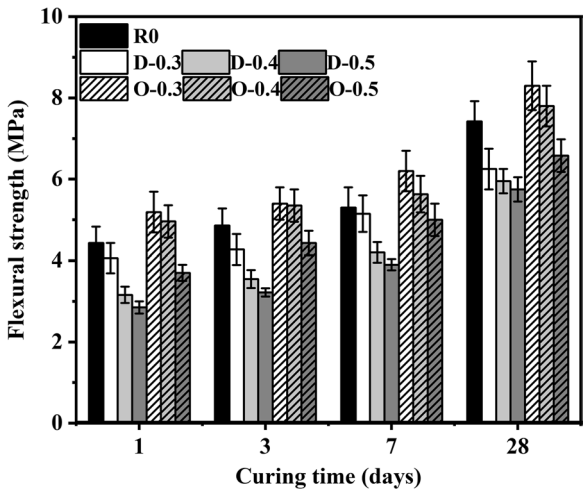

Fig. 16 Flexural strength of the mortar with different aggregates

composite ratios shows an improvement of 14.4–32.8% over the pre-optimization. The reason for the increase in flexural strength is similar to that of compressive strength, i.e., grading optimization enhances the filling of structural pores. The 28-day flexural strengths of O-0.3 and O-0.4 were 8.30 MPa and 7.80 MPa, respectively, which were 11.9 and 5.1% higher than the flexural strengths of R0 mortar, however, the 28-day flexural strength value of O-0.5 was 6.58 MPa, and its flexural strength did not exceed the control R0 at all ages and was 11.3% lower than the control at 28 days.

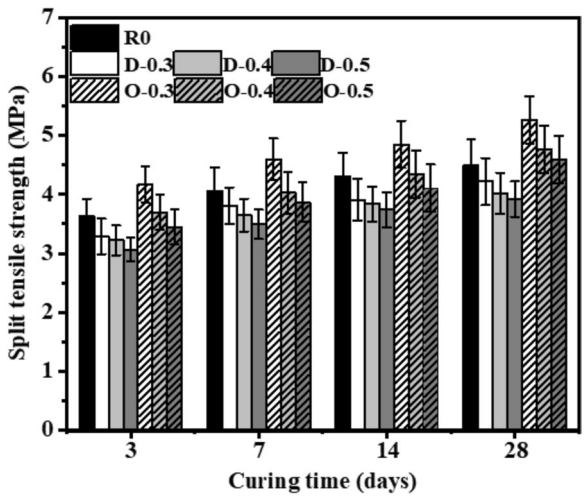

Fig. 17 Split tensile strength of the mortar for both the direct and optimized mixes

3.4 Split Tensile Strength

Split tensile strength was tested for all mortar sequences on days 3, 7, 14 and 28 and the results are shown in Fig. 17. The split tensile strength of control R0 at days 3, 7, 14, and 28 was 3.63, 4.06, 4.31, and 4.49 MPa, respectively. The split tensile strengths of D-0.3, D-0.4, and D-0.5 were 6.0, 10.5, and 12.7% lower than that of the control at 28 days. When α was raised from 0.3 to 0.5, the split tensile strength of the specimens at 28 days of age decreased from 4.22 MPa to 3.92 MPa (−7.1%).

The split tensile strengths of optimized graded composite aggregate mortar sequences O-0.3, O-0.4 and O-0.5 at 3, 7, 14 and 28 days ranged from 3.45–4.17, 3.87–4.61, 4.11–4.85, to 4.59–5.27 MPa. The development of split tensile strength of the gradation optimized combination aggregate mixtures at 3, 7, 14 and 28 days showed 4.2–12.9%, 4.7–11.7%, 4.3–11.1% and 2.3–14.9% improvement in strength compared to the control R0, respectively. When the aggregate gradation is properly distributed, a more uniform and continuous particle skeleton can be formed, which is conducive to the uniform distribution of stress realization and the reduction of stress concentration, thus improving the splitting tensile properties of the material (Bai, Wang, Ma, Sanjayan, & Bai, 2021; Kong et al., 2023).

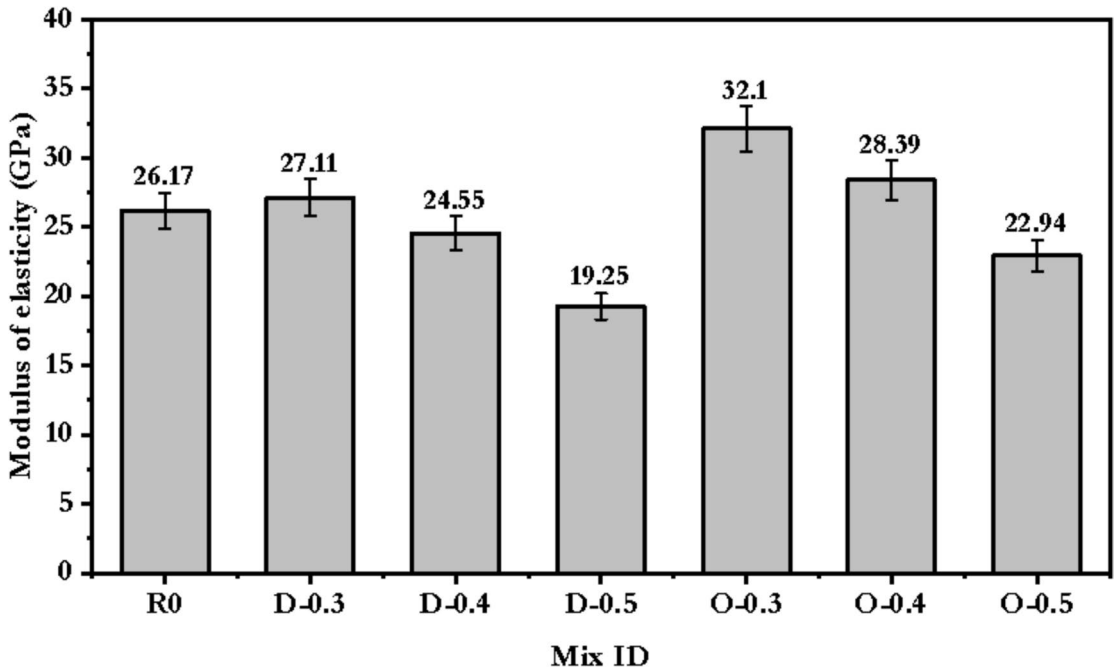

Fig. 18 Elastic modulus of the direct and optimised concrete mixes at 28 d

3.5 Elastic Modulus

The modulus of elasticity is an important parameter for measuring the stiffness of a material, which reflects its ability to resist deformation when subjected to external forces. The modulus of elasticity was tested at day 28 for all mortar test sequences and the results are shown in Fig. 18. The 28-day modulus of elasticity of the control R0 was 26.17 GPa. For the direct-mixed composite aggregate, the 28-day modulus of elasticity value of D-0.3 was 27.11 GPa, which is 3.0% higher than that of R0. However, the modulus of elasticity of the mortar decreased significantly with increasing α, showing a developmental pattern similar to that of the compressive strength, with the 28-day modulus of elasticity of 24.55 GPa and 19.25 GPa for the D-0.4 and D-0.5 test sequences, respectively, which decreased by 9.4 and 29.0%, respectively, compared to D-0.3, and were inferior to the control mortar by 6.2 and 26.4%, respectively.

Figure 18 shows that the 28-day modulus of elasticity of the gradation-optimized test mortar sequences showed 15.6–19.2% improvement over the pre-optimization at different composite ratios. When the gradation of DS and FS aggregates was improved, the cement hydration in the mortar was sufficient and the dense aggregate particles provided better force deformation properties and enhanced the elastic modulus of the mortar (Duan et al., 2021). The 28-day modulus of elasticity of O-0.3 and O-0.4 was 32.10 GPa and 28.39 GPa, respectively, which were 22.7% and 8.5% higher than that of the control R0 mortar, and O-0.5 was 22.94 GPa, which was 12.3% lower than the control.

4 Microstructural Analysis

Literature has shown that pores in cement pastes can be categorized into three main groups based on their size, i.e., macropores (>50 nm), mesopores (2–50 nm), and micropores (<2 nm) (Le et al., 2015). For different pore sizes, several test methods can be used (Song et al., 2019, 2020). The image recognition method based on ImageJ software has been shown to have high accuracy in characterizing parameters such as radius, area, circularity and porosity of medium, and large pores above 5 nm. For example, Neithalath et al. carried out a comparison of planar porosity measured using this method with volumetric porosity measured by the conventional drainage method on permeable concrete samples, and the two results were well fitted with an average error rate of 9.7% (Neithalath et al., 2010). Shafaei evaluated both 2D and 3D porosity using this method on mortar samples mixed with titanium dioxide cement with an average error rate of 13.0% and a consistent pattern (Shafaei et al., 2020). Therefore, we used ImageJ software for SEM images and calculated the porosity by the ratio of the number of pore pixels obtained by software recognition to the total number of pixels in the image. The SEM images and porosities of different materials are shown in Fig. 19a–g, the observation area was set to be the cement paste body, since the damage mode of mortar under pressure was all cementite cracking damage, rather than damage in the interfacial transition zone.

Figure 19a indicates that the R0 sample has a uniform and dense microstructure, with almost no large pores and visible cracks, and the largest pores are around 5 μm. Figure 19b shows that the sample using D-0.3 still has a relatively dense microstructure, without observable microcracks, and only a few medium-sized pores around 20 μm. Figure 19c shows that the surface cracks appeared and the size of cracks and pores in the D-0.4 sample increased, more medium-sized pores of about 20 μm and several dispersed cracks of about 80–100 μm in length can be observed. Figure 19d shows that sample D-0.5 has a very large number of pores and loose parts, and a penetrating crack of about 300 μm in length is observed. The porous and cracked microstructure significantly affects the macro mechanical properties of the mortar, which is proven by the mechanical test results. One of the main reasons for the poor microstructures of D-0.4 and D-0.5 is that the high percentage of DS becomes the main aggregate of the mortar and fails to optimize the interstitial effect of the grading, which substantially increases the specific surface area of the aggregate and reduces the thickness and densification of the mortar. Figure 20 summarizes the porosity of the mortar obtained after thresholding the images in greyscale and identifying them, where the porosity of R0 is 5.38%, and the porosity of D-0.3, D-0.4, and D-0.5 are 5.68, 6.86, and 7.97%, respectively, which are 5.6, 27.5, and 48.1% higher than that of the control group, respectively. The densification degree of the sample micro-morphology is consistent with the results of the porosity.

Figure 19e–g show the SEM images of the samples O-0.3, O-0.4 and O-0.5 after grade optimization. Figure 19e shows that the O-0.3 sample has a very dense surface almost without visible larger pores and cracks, and the pores around 20 μm are significantly reduced compared to the pre-optimization sample. Figure 19f shows that a pair of penetrating cracks of about 200 μm and a certain number of non-penetrating cracks with lengths of less than 80 μm appear on the surface of the O-0.4 sample, however the medium-sized pores of 20 μm are reduced compared to the pre-optimization case. Figure 19g shows that the surface of O-0.5 still has more large-sized pores, and the long penetrating cracks disappear compared to the pre-optimization, but many scattered fine cracks are also observed. Overall, the pores

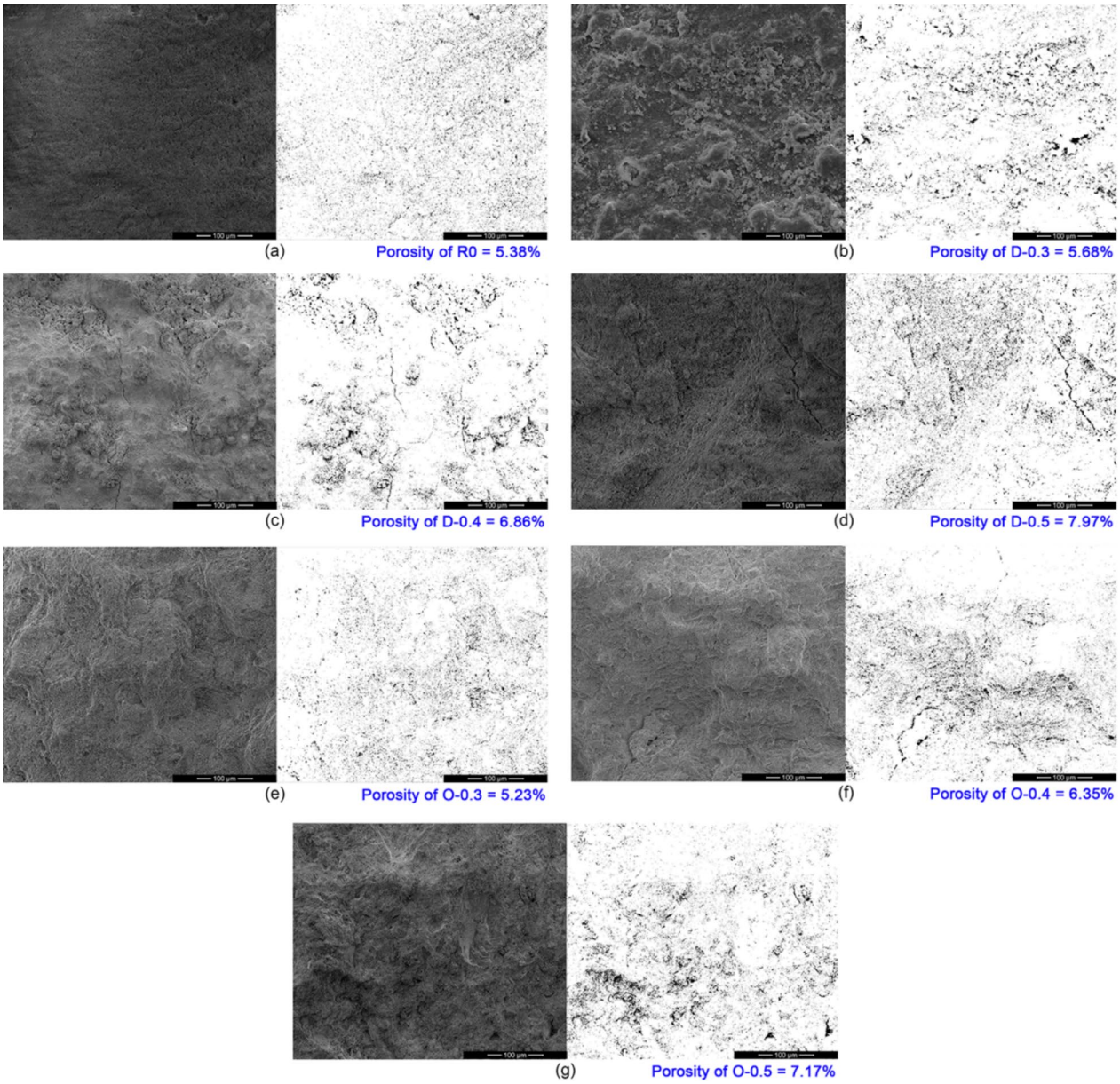

Fig. 19 SEM images of 28 d mortar samples and images processed with grayscale threshold: **a** R0 **b** D-0.3 **c** D-0.4 **d** D-0.5 **e** O-0.3 **f** O-0.4 g O-0.5

and cracks of the gradation-optimized samples were improved compared to the pre-optimization samples, and the microstructure of the cement mortar is denser. The results of porosity estimated by ImageJ software showed that the porosity of O-0.3, O-0.4, and O-0.5 samples were 5.23%, 6.35%, and 7.17%, respectively, which decreased by 7.4–10% compared with that before optimization. The results of SEM-based microphysical observations and greyscale threshold-based analysis provide consistent evidence for change in mechanical strength.

The pore size distribution (PSD) curves were obtained by applying thresholding to Fig. 19 using ImageJ, as shown in Fig. 21. Due to the fact that only pores equal to, or larger than 1 pixel in the image can be identified, the minimum diameter of the identified pores is 0.38 μm. The pores with a diameter range of 0.38–0.85 μm in all series of samples were representative, accounting for 60.0–81.3% of all pores. The proportion of composite aggregate had a significant effect on the distribution of pore diameters. The R0, O-0.3, and O-0.4 samples have a higher proportion of small pore sizes within the range

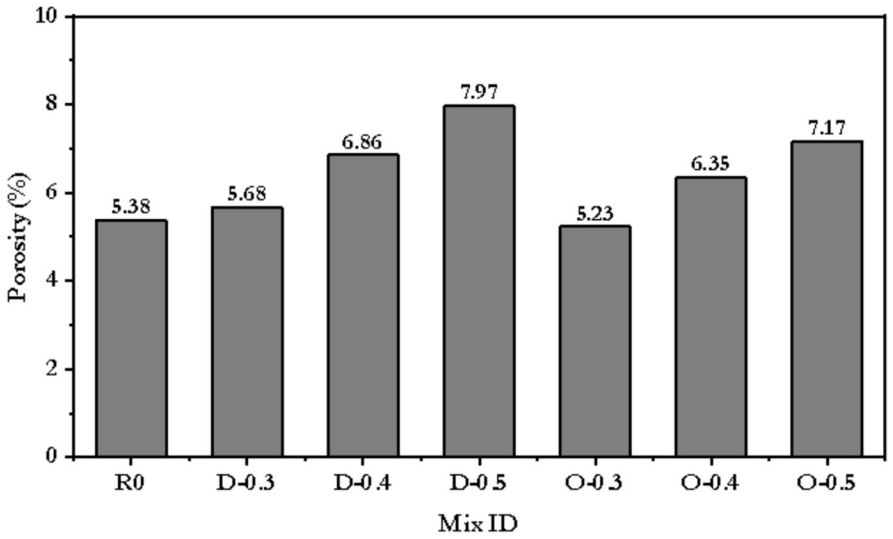

Fig. 20 Porosity of SEM images of 28 d mortar sample

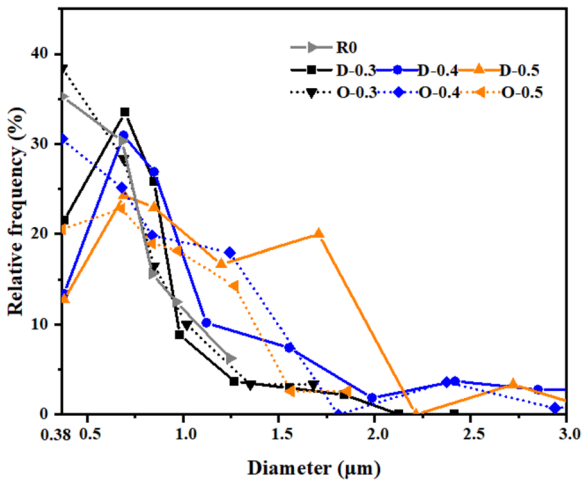

Fig. 21 Size pore distribution of structural mortars specimens' section (SEM images)

of 0.38–0.7 μm, reaching over 30.4%, while the proportion of other samples within this pore size range does not exceed 21.5%. As the composite ratio α increased, the number of small pores with diameters less than 1.0 μm decreased and the percentage of large pores with diameters greater than 1.0 μm increased significantly in the samples. Compared with the samples before grading optimization, the relative frequency of pores larger than 1.0 μm in diameter in O-0.3, O-0.4 and O-0.5 samples decreased by 4.1–12.1%, indicating that grading optimization can reduce the large diameter capillary pores.

Figure 22 demonstrates the bonding interfaces between aggregate and cement paste of R0, D-0.3, D-0.4 and D-0.5 samples. Figure 22a shows that in the R0 sample, the bonding between RS and paste is better, and the widest crack at the interface is about 3 μm. As shown in Fig. 22b, for the D-0.3 sample, the bonding between FS and paste is perfect, and there is almost no visible defect, attributed to the fact that FS has sharp edges and rougher surface texture which is favourable to the adhesion between aggregate and paste (Das et al., 2023; Islam et al., 2021). Another reason for the good bonding is that FS has a porous structure, and the water released from the pores of FS migrates to the hardened cement paste at the late stage of hydration, forming a micro-hydration environment that promotes the hydration reaction, and the generation of additional hydration products makes the aggregate-paste interface denser (Zhu et al., 2023). In addition, DS embedded in FS particles was observed to play a filling effect. The effects of local moisture release and filling between aggregates are demonstrated in Fig. 23. The porous structure of FS aggregates releases moisture during the later stage of hydration, creating a micro-hydration environment in the local interfacial zone, promoting the formation of hydration products, and enhancing the bond between aggregates and paste. It can be observed from Fig. 22c that the aggregate-paste interface of the D-0.4 samples had discontinuous cracks with a widest width of about 15 μm. Figure 22d shows that the interface quality of sample D-0.5 is significantly compromised due to the presence of penetrating narrow cracks with a maximum width of about 15 μm. This may be due to the high content of DS components with high specific surface area, which makes the hydration reaction proceed incompletely and thus prevents the

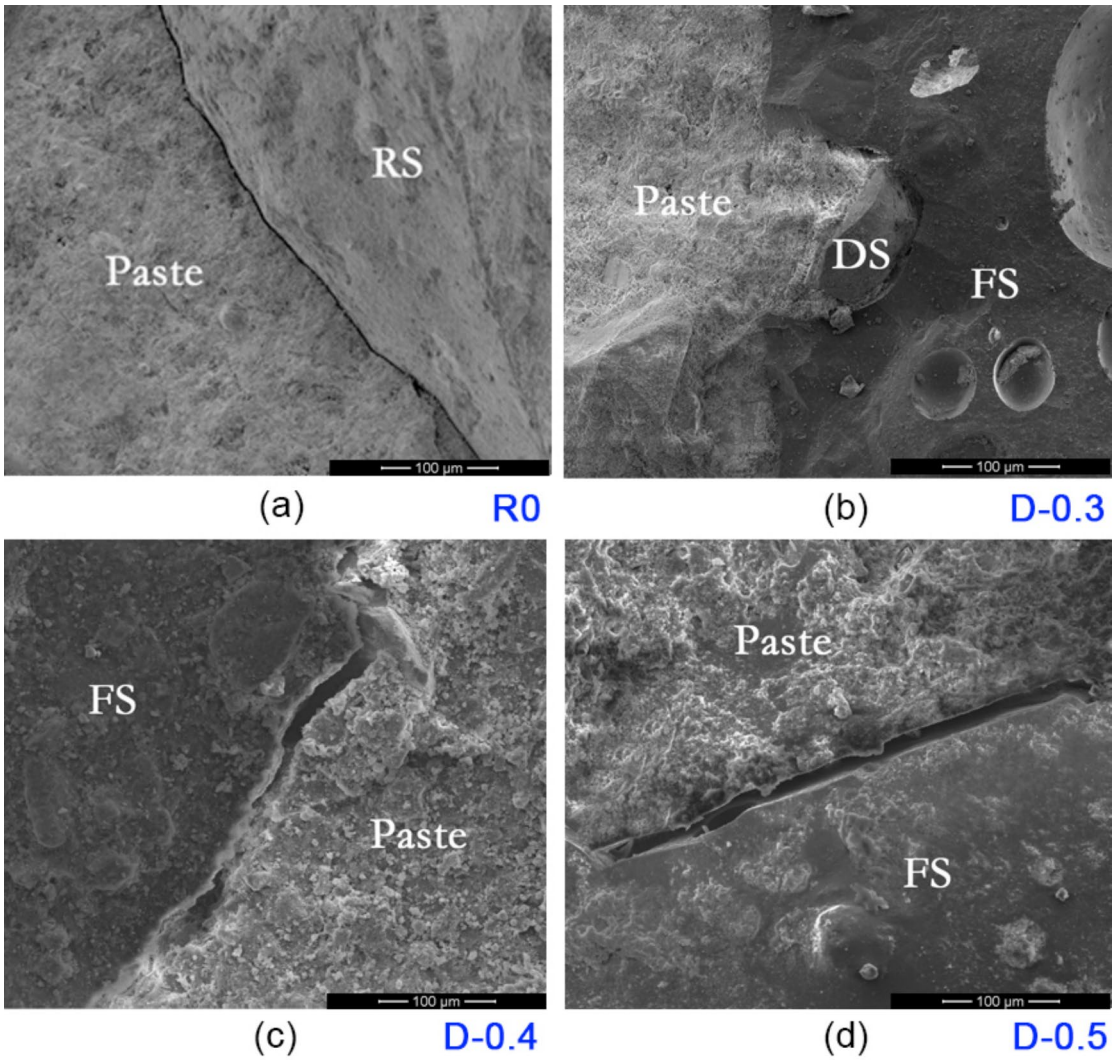

Fig. 22 SEM images of the interface between aggregate and cement paste of 28 d mortar samples: **a** R0 **b** D-0.3 **c** D-0.4 **d** D-0.5

formation of hydration products in the pore structure at samples D-0.4 and D-0.5.

The microstructures of the hydration products of R0, D-0.3, D-0.4, and D-0.5 were displayed in Fig. 24, in which the types of hydration products were determined based on a combination of morphology and EDS analyses. Figure 24a shows that very abundant needle-and-rod AFt crystals were found on the R0 sample of the control mortar, which was dispersed in a randomly oriented pattern, intertwined into an overall network, and densified the microstructure of the mortar through microscale enhancement and filling effects. Figure 24b shows that the needle-and-rod AFt crystals are also present in the D-0.3 sample, but with a lower number and thickness than the R0 sample. In addition, a certain number of flocculated C-S-H crystals were also observed, as FS is rich in calcium oxide and magnesium oxide, which react with the cement to form additional calcium and magnesium hydrate products (Das et al., 2023). It can be found from Fig. 24c that the needle-and-rod AFt crystals could no longer be detected in sample D-0.4, and only a certain number of flocculated C-S-H crystals can be observed, as well as a few flaky CH crystals. Figure 24d shows that only a few dispersed flaky CH crystals are present in the D-0.5 sample, indicating that a high percentage of DS prevents the growth of cement hydration products. CH crystals have low strength and are easily broken under external force, thereby contributing to strength degradation of D-0.4 and D-0.5 samples.

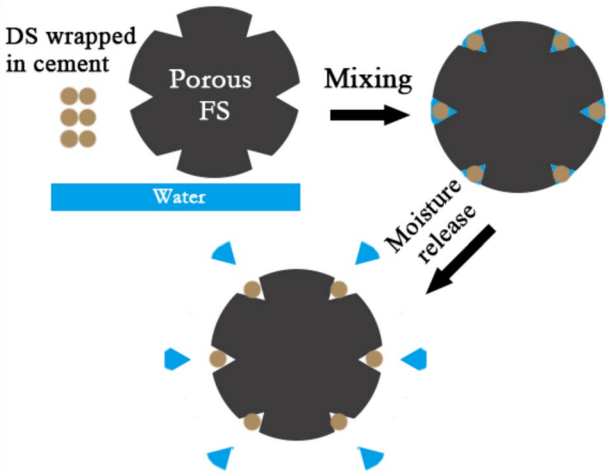

Fig. 23 Local moisture release and filling effects caused by porous FS aggregates

5 Evaluations of Economy and Embodied Environmental Impact

The total cost and cost efficiency (C_p) of different test sequences are shown in Fig. 25. To simplify the analysis, materials contributing less than 1% to C_p have been omitted from the chart. As depicted in Fig. 25, the total cost and C_p value for mortar using RS as aggregate are 111.30 USD/m^3 and 2.41 USD/m^3·MPa, respectively. In contrast, using DS and FS as substitute aggregates can reduce the total cost by 31.3–32.7% and the C_p value by 8.3–46.9%. The reduction in total cost is attributed to the lower cost of novel aggregates, while the decrease in C_p value results from a combination of reduced aggregate costs and enhanced compressive strength. Moreover, as the α value increases, the C_p value of the new aggregate mortar shows an upward trend, mainly due to the decrease in compressive strength. Notably, although grading optimization did not significantly change the total cost of raw materials, it achieved a significant reduction in the C_p value in optimized gradation sequences by 17.2–19.2% through improving the compressive strength of the mortar, further highlighting the economic benefits of grading optimization.

The total potential carbon emission ($\sum ECO_2$) and the ECO_2 efficiency (*CI*) of different test sequences are shown in Fig. 26. Similarly, materials contributing less than 1% to *CI* have been omitted from the chart. As depicted in Fig. 26, the total potential carbon emission and *CI* value for mortar using RS as aggregate are 318.79 kg/m^3 and 6.90 kg/m^3·MPa, respectively. Compared to RS, using DS and FS as aggregate for replacement results in lower ECO_2 emissions from the extraction, processing, and transportation phases, leading to a decrease in total potential carbon emission by 6.4%. At α = 0.3, the composite aggregate mortar exhibits a lower *CI* value than the control group, with D-0.3 and O-0.3 being 11.9 and 27.7% lower, respectively. However, as α increases from 0.3 to 0.5, despite minimal change in total potential carbon emissions, the *CI* values of mortar produced from composite aggregates before and after grading

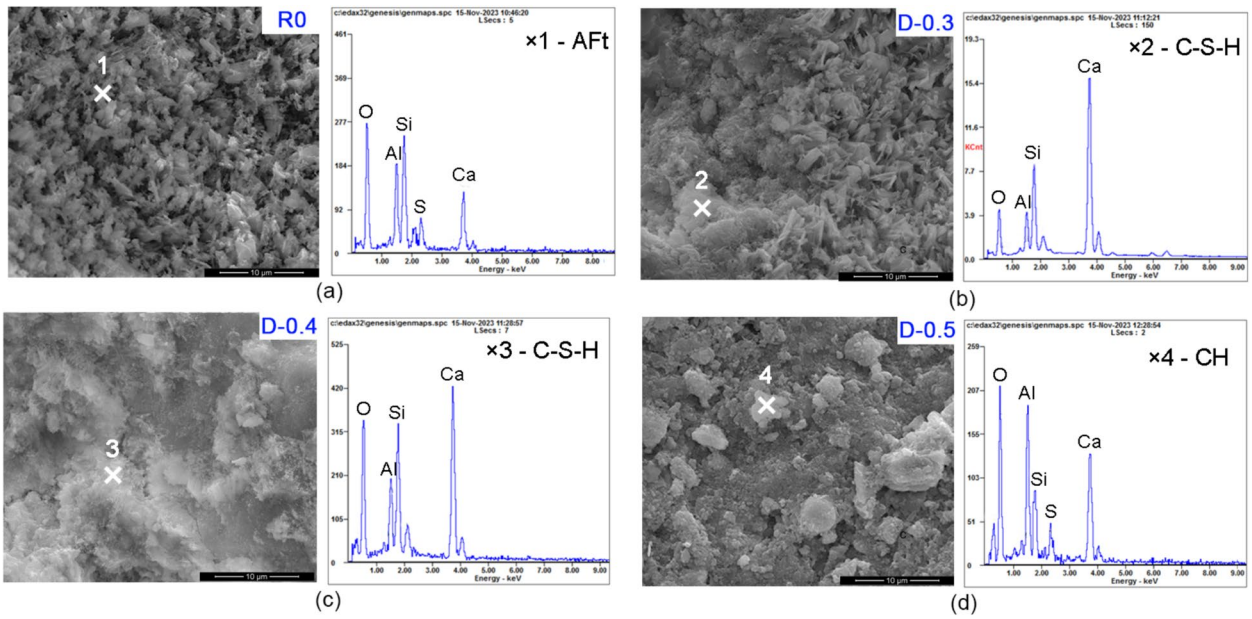

Fig. 24 SEM images of hydration products of 28 d mortar samples: **a** R0 **b** D-0.3 **c** D-0.4 **d** D-0.5

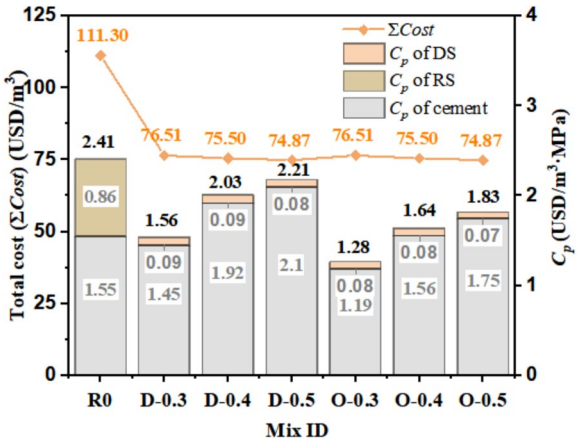

Fig. 25 Cost Efficiency of the mortar with different aggregates

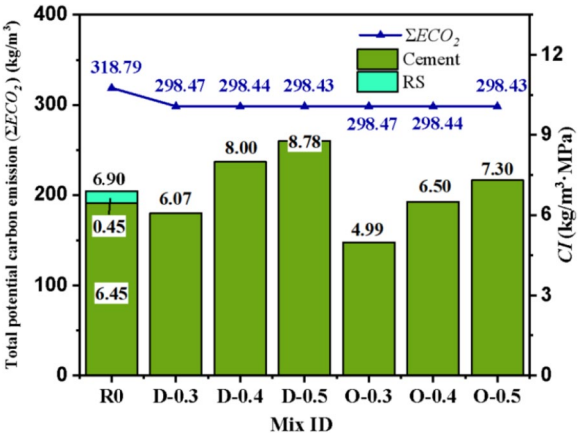

Fig. 26 ECO_2 emission index of the mortar with different aggregates

optimization increase by 44.6 and 46.3%, respectively, due to the marked decrease in compressive strength. This demonstrates the potential contribution of grading optimization in reducing environmental impact.

6 Statistical Analysis and Comprehensive Evaluation

To explore the interrelationships among performance indicators of composite aggregate mortars, a statistical analysis was performed. The Pearson proximity matrices for flowability, compressive strength, flexural strength, split tensile strength, and porosity are shown in Fig. 27. Among the positive correlations, the relationship between flexural strength and split tensile strength is the strongest, with a correlation coefficient of 0.938. This may be attributed to the similarity in their failure mechanisms, both dominated by interfacial cracking. In contrast, the positive correlation between flowability and compressive strength is the weakest, with a coefficient of 0.765, possibly because flowability is more influenced by the characteristics of the fresh paste, while compressive strength primarily depends on the compactness and interfacial bonding after hardening. Among the negative correlations, the relationship between porosity and compressive strength is the strongest, with a correlation coefficient of −0.875. This is due to the direct impact of porosity on mortar compactness, where higher porosity leads to increased internal defects, significantly reducing the mortar's ability to withstand compressive loads. In comparison, the negative correlation between porosity and split tensile strength is the weakest, with a coefficient of −0.616, likely because split tensile strength is more influenced by aggregate interfacial properties and stress distribution, and is relatively less sensitive to internal porosity.

The statistical analysis indicates that performance indicators with strong positive correlations, such as flexural strength and split tensile strength, reflect similarities in their stress mechanisms. Meanwhile, in negative correlations, the strong inverse relationship between porosity and compressive strength highlights the critical role of compactness on compressive performance. These analyses provide further basis for optimizing the mix proportions of composite aggregate mortars.

Building on the insights from the statistical analysis, a comprehensive evaluation of the performance of alternative aggregate sequences was conducted using a six-dimensional radar diagram, as shown in Fig. 28. This diagram plots the relationships of flowability, compressive strength, elastic modulus, porosity, ECO_2 emission, and cost efficiency, with the latter three represented by their reciprocals. The values in the radar diagram represent the ratios of each experimental sequence and control group (R0) for a given parameter. Figure 28a shows that D-0.3 mortar is superior to R0 in the indicators of compressive strength, modulus of elasticity, ECO_2 emission (reciprocal) and cost efficiency, which are increased by 8.4, 3.6, 13.5 and 54.6% respectively; but in terms of flowability and porosity (reciprocal), 13.5% and 5.3% lower than R0, respectively. As the aggregate composite ratio α increases, all the indices show a decreasing trend. D-0.4 is lower than R0 by 6.2–21.6% in each performance index except for cost efficiency, and D-0.5 is lower than R0 by 21.5–32.5% in each performance index, except for cost efficiency (see Fig. 28b, c). After aggregate grading optimization, the six-dimensional indices of the samples with different composite ratios are improved to different degrees. For O-0.3 samples, except for a slightly lower flowability of 2.3% compared to R0, other performance indices were improved by 2.9–89.4% as compared with the control group, as shown in Fig. 28a. The O-0.4 sample is better than the control group in elastic modulus, ECO_2

Pearson's Correlations	Flowability	Compressive strength	Flexural strength	Split tensile strength	Porosity
Flowability	1.000				
Compressive strength	0.765	1.000			
Flexural strength	0.879	0.812	1.000		
Split tensile strength	0.803	0.843	0.938	1.000	
Porosity	-0.824	-0.875	-0.704	-0.616	1.000

+1.000 +0.765 -0.616 -1.000

Fig. 27 Pearson proximity matrices for flowability, compressive strength, flexural strength, split tensile strength, and porosity

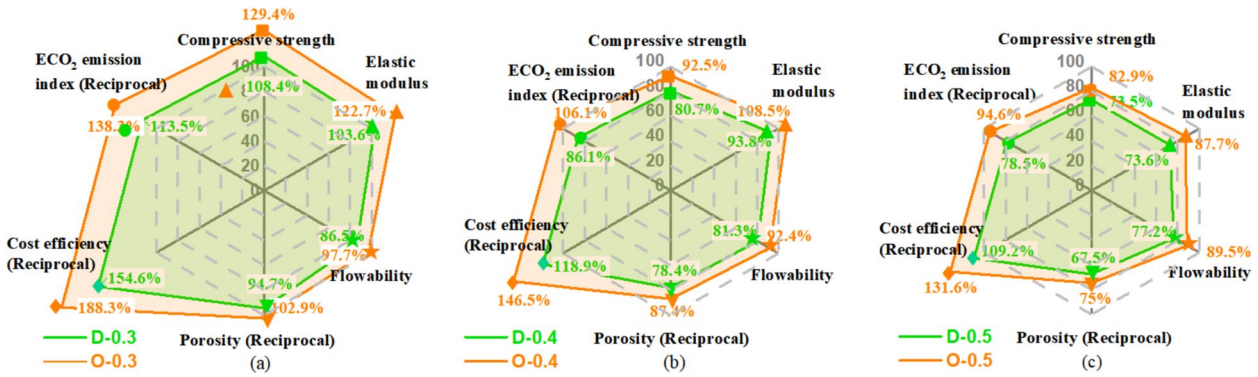

Fig. 28 Radar diagram depicting performance of mortar with respect to replacement of DS and FS:**a** D-0.3 and O-0.3; **b** D-0.4 and O-0.4; **c** D-0.5 and O-0.5

emission, and cost efficiency, however, its compressive strength, flowability and porosity were inferior to the control group, those were decreased by 7.5–12.6%, especially the porosity was 12.6% lower than that of the control group, as shown in Fig. 28b. Figure 28c shows that, for the O-0.5 sample, although its aggregate grading was optimized, its indices were far lower than that of the control group except for the cost efficiency, indicating that the ratio of DS and FS is not suitable.

In terms of mechanical strength, the most unfavourable group using the new composite aggregate is the D-0.5 sequence, whose 7 d and 28 d compressive strengths were 15.29 MPa and 33.95 MPa respectively. The compressive strengths of all mortar sequences meet the ASTM C1329 (2016) specification, as shown in Fig. 29. Improved flowability benefits better plasticity and concrete pouring. However, for 3D printing concrete, the suitable flowability ranges from 140 to 210 mm (Ma et al., 2018; Tay et al., 2019). As shown in Fig. 29, the material flowability of D-0.3, O-0.3, O-0.4, and O-0.5 meets the requirement of 3D printing. The direct use of mortars D-0.4 and D-0.5 for 3D printing may lead to quality degradation, to improve the flowability of these two mixes, additives like high-efficiency water-reducing and dispersing agents should be incorporated (Rahul et al., 2019). As for economic benefits, all the new composite aggregates exhibit significantly higher economic efficiency compared to

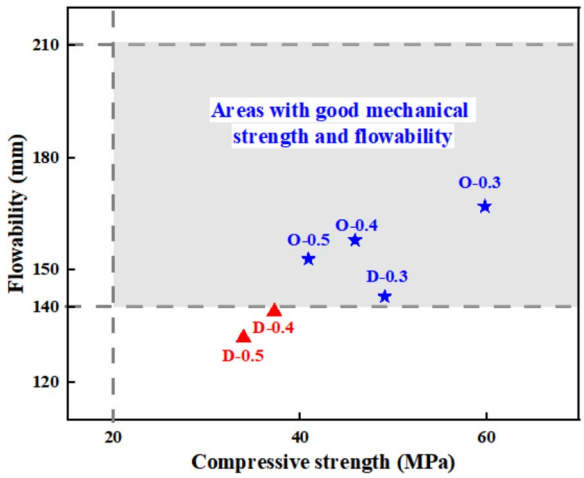

Fig. 29 Optimal compressive strength and flowability range of mortar suitable for 3D printing

R0, with reductions in the cost (C_p) ranging from 8.5 to 46.9%. When considering the costs associated with solid waste processing, these economic benefits are even more pronounced. In addition, when α is low, the test sequence can exhibit lower ECO_2 emission index (*CI*) than the control group. Thus, the new composite aggregates provide a balanced approach, achieving substantial economic gains while maintaining reasonable environmental impact, especially in the case of the D-0.3 and O-0.3 sequence. In this study, FS was used as fine aggregate replacement rather than cement, resulting in small *CI* reductions, which become higher than the control group at higher α values. If FS is ground into ash and used as a partial replacement for cementitious materials, it could effectively reduce the *CI* values, thereby achieving truly low-carbon and environmentally friendly materials. This approach will be further explored in future studies to enhance environmental sustainability.

Although the above evaluations cover mechanical, economic, and environmental performance, durability, a crucial factor, was not addressed in this study. At the chemical level, the amorphous phases present in DS and FS participate in pozzolanic reactions to generate additional C-S-H gel. This process is similar to the mechanism of supplementary cementitious materials reported by Panda et al. (PANDA et al., 2024a, 2024b), enhancing the matrix's resistance to acid and sulfate attack through the formation of stable hydration products. At the physical structure level, the combination of DS and FS exhibits a unique synergistic effect: the fine DS particles (D50 = 0.15 mm) effectively fill the porous structure of FS to reduce the overall porosity of the system, while the rough surface and internal pore structure of FS may inhibit chloride ion diffusion through dual mechanisms of physical adsorption and pore blockage (Nanda et al., 2025). This synergistic effect is expected to significantly improve the material's impermeability (Nanda et al., 2025).

However, in the absence of specific experimental data, the above assumptions remain speculative and require further validation through experimental results. Future studies will incorporate durability tests to verify these hypotheses and comprehensively evaluate the long-term performance of DS and FS composite aggregates.

7 Conclusion

This study systematically investigated the complete replacement of river sand with optimized composite aggregates consisting of dune sand (DS) and ferrochrome slag (FS) for sustainable mortar production. The flowability, compressive strength, flexural strength, splitting tensile strength, modulus of elasticity, and microstructural properties of the new mortar have been examined and compared with the control group. The following conclusions can be drawn from the test results:

1. The flowability of mortars made with composite aggregates decreased with increasing DS content, exhibiting values 2.4–29.5% lower than the reference mix. This reduction is attributed to both the higher specific surface area of fine DS particles requiring more cement paste for lubrication and the lower sphericity and circularity of FS particles increasing frictional resistance. Grading optimization reduced particle gaps and friction between mortar components, improving flowability by 12.8–15.9% for the same composite ratio.
2. At the age of 28d, mortar containing 30% DS and 70% FS demonstrated optimal compressive strength reaching 59.8 MPa, exceeding the control group by 8.4%, while the 50% DS and 50% FS mixture showed the lowest strength at 33.95 MPa, falling 26.5% below control values. Grading optimization significantly enhanced mechanical properties, improving 28-day compressive strength by 20.5–23.2% and flexural strength by 14.4–32.8%, primarily attributed to reduced internal porosity and improved interfacial transition zones between aggregates and cement matrix.
3. SEM analysis showed that the porosity of the mortar increased with the increase in the mass percentage of DS in the aggregate. The grading-optimized samples showed a denser surface with richer hydration products under the microscope, and the pores and cracks

were significantly reduced compared with those before optimization. The results of porosity analysis showed that the porosity of the gradation-optimized samples decreased by 7.4–10%. This exhibits a consistent regularity with the results of mechanical strength.

4. Optimizing the use of DS and FS as alternative aggregates significantly reduces costs and potential carbon emissions. The C_p and CI values of sequence O-0.3 decreased by 47.3 and 27.7%, respectively, compared to the control group. This improvement stems from the low-cost DS and zero-cost FS as an industrial by-product compared to traditional river sand, with a reduced environmental footprint during extraction and processing. FS could be further utilized as a cementitious replacement material to enhance sustainability.
5. The results of the comprehensive performance evaluation showed that all the indices tended to decrease with the increase in composite ratio. However, the optimized grades improved the performance, and five performance indices of the mortar made of optimized grades of 30% DS and 70% FS are significantly better than the control group. The strength of all mixes met the requirements of the ASTM C1329 specification, however, the flowability of mortars D-0.4 and D-0.5 needs to be improved to meet the requirements of 3D printing.

Acknowledgements
The authors sincerely acknowledge the financial support from the National Natural Science Foundation of China, Shanxi-Zheda Institute of New Materials and Chemical Engineering, R&D Program of Zhejiang Province, R&D Program of Guangxi Province, and the technical assistance provided by the Centre for Balance Architecture at Zhejiang University.

Author Contributions
H.W.: Conceptualization, Methodology, Funding acquisition, Investigation, Supervision, Validation, Visualization, Writing—original draft, Writing—review and editing. J.S.: Methodology, Investigation, Visualization, Writing—original draft. X.S.: Conceptualization, Methodology, Funding acquisition, Investigation, Supervision, Validation, Writing—review and editing. Q.S.: Writing—review and editing. W.D.: Formal analysis, Resources. All authors read and approved the final manuscript.

Funding
This work was supported by National Natural Science Foundation of China (52279141, 52478284), Shanxi-Zheda Institute of New Materials and Chemical Engineering (2022SZ-TD016), R&D Program of Zhejiang Province (2023C01154, 2022C04005, and 2021C01022), R&D Program of Guangxi Province (AB22035031).

Data Availability
The datasets used and/or analyzed during the current study are available from the corresponding author on reasonable request.

Declarations

Ethics Approval and Consent to Participate
Not applicable.

Consent for Publication
Not applicable.

Competing interests
The authors declare that they have no competing interests.

Received: 6 March 2025 Accepted: 16 July 2025
Published online: 18 September 2025

References

Abu Seif, E.-S.S., Sonbul, A. R., Hakami, B. A. H., & El-Sawy, E. (2016). Experimental study on the utilization of dune sands as a construction material in the area between Jeddah and Mecca, Western Saudi Arabia. *Bulletin of Engineering Geology and the Environment, 75*, 1007–1022. https://doi.org/10.1007/s10064-016-0855-9

Achour, R., Zentar, R., Abriak, N.-E., Rivard, P., & Gregoire, P. (2019). Durability study of concrete incorporating dredged sediments. *Case Studies in Construction Materials, 11*, Article e00244. https://doi.org/10.1016/j.cscm.2019.e00244

Al-Jabri, K., Shoukry, H., Khalil, I. S., Nasir, S., & Hassan, H. F. (2018). Reuse of waste ferrochrome slag in the production of mortar with improved thermal and mechanical performance. *Journal of Materials in Civil Engineering, 30*(8), 04018152. https://doi.org/10.1061/(ASCE)MT.1943-5533.0002345

Alsharif, W., Saad, M. M., & Hirt, H. (2020). Desert microbes for boosting sustainable agriculture in extreme environments. *Frontiers in Microbiology, 11*, Article 496411. https://doi.org/10.3389/fmicb.2020.01666

ASTM C1437-15: Standard Test Method for Flow of Hydraulic Cement Mortar. (2015). *ASTM International, West Conshohocken, PA*.

ASTM C128: Standard Test Method for Relative Density (Specific Gravity) and Absorption of Fine Aggregate. (2015). *ASTM International West Conshohocken, PA*.

ASTM C29: Standard Test Method for Bulk Density ("Unit Weight") and Voids in Aggregate. (2017). *ASTM International, West Conshohocken, PA*.

ASTM C496: Standard Test Method for Splitting Tensile Strength of Cylindrical Concrete Specimens. (2017). *ASTM International, West Conshohocken, PA*.

ASTM C33: Standard Specification for Concrete Aggregates. (2019). *ASTM International, West Conshohocken, PA*.

ASTM C348: Standard test method for flexural strength of hydraulic-cement mortars. (2019). *ASTM International, West Conshohocken, PA*.

Attri, G. K., Gupta, R. C., & Shrivastava, S. (2022). Comparative environmental impacts of recycled concrete aggregate and manufactured sand production. *Process Integration and Optimization for Sustainability, 6*(3), 737–749. https://doi.org/10.1007/s41660-022-00244-4

Bai, G., Wang, L., Ma, G., Sanjayan, J., & Bai, M. (2021). 3D printing eco-friendly concrete containing under-utilised and waste solids as aggregates. *Cement and Concrete Composites, 120*, Article 104037. https://doi.org/10.1016/j.cemconcomp.2021.104037

Behera, M., Minocha, A., & Bhattacharyya, S. (2019). Flow behavior, microstructure, strength and shrinkage properties of self-compacting concrete incorporating recycled fine aggregate. *Construction and Building Materials, 228*, Article 116819. https://doi.org/10.1016/j.conbuildmat.2019.116819

Chinyama, S. R., Wenga, T., & Gwenzi, W. (2023). Mechanical and contaminant leaching behaviour of cement-based and fired bricks incorporating ferrochrome slag. *Journal of Building Engineering, 72*, Article 106572. https://doi.org/10.1016/j.jobe.2023.106572

Cui, G., Liu, J., Yao, T., & Lin, W. (2010). Mix proportion design of reactive powder concrete based on Dinger-funk equation. *Journal of Southeast University. Natural Science Edition, 40*, 1.

Damene, Z., Goual, M., Houessou, J., Dheilly, R. M., Goullieux, A., & Quéneudec, M. (2018). The use of southern Algeria dune sand in cellular lightweight concrete manufacturing: Effect of lime and aluminium content on

porosity, compressive strength and thermal conductivity of elaborated materials. *European Journal of Environmental and Civil Engineering, 22*(10), 1273–1289. https://doi.org/10.1080/19648189.2016.1256233
Das, S., Patra, R. K., & Mukharjee, B. B. (2021). Feasibility study of utilisation of ferrochrome slag as fine aggregate and rice husk ash as cement replacement for developing sustainable concrete. *Innovative Infrastructure Solutions, 6*, 1–18. https://doi.org/10.1007/s41062-021-00461-9
Das, S. K., Tripathi, A. K., Kandi, S. K., Mustakim, S. M., Bhoi, B., & Rajput, P. (2023). Ferrochrome slag: A critical review of its properties, environmental issues and sustainable utilization. *Journal of Environmental Management, 326*(Pt A), Article 116674. https://doi.org/10.1016/j.jenvman.2022.116674
Dash, M. K., & Patro, S. K. (2018). Effects of water cooled ferrochrome slag as fine aggregate on the properties of concrete. *Construction and Building Materials, 177*, 457–466. https://doi.org/10.1016/j.conbuildmat.2018.05.079
De Larrard, F., & Sedran, T. (1994). Optimization of ultra-high-performance concrete by the use of a packing model. *Cement and Concrete Research, 24*(6), 997–1009. https://doi.org/10.1016/0008-8846(94)90022-1
Dinger, D. R., & Funk, J. E. (1997). Particle-packing phenomena and their application in materials processing. *Mrs Bulletin, 22*(12), 19–23. https://doi.org/10.1557/S0883769400034692
Dinh, H. L., Liu, J., Ong, D. E. L., & Doh, J. H. (2022). A sustainable solution to excessive river sand mining by utilizing by-products in concrete manufacturing: A state-of-the-art review. *Cleaner Materials, 6*, Article 100140. https://doi.org/10.1016/j.clema.2022.100140
Duan, Z., Li, B., Xiao, J., & Guo, W. (2021). Optimizing mix proportion of recycled aggregate concrete by readjusting the aggregate gradation. *Structural Concrete, 22*, E22–E32. https://doi.org/10.1002/suco.201900517
El-Hassan, H., Alnajjar, F., Al Jassmi, H., & Ahmed, W. (2020). Fresh and hardened properties of 3D-printed concrete made with dune sand. *Paper Presented at the Second RILEM International Conference on Concrete and Digital Fabrication: Digital Concrete, 2020*, 2.
Elibol, C., & Sengul, O. (2016). Effects of activator properties and ferrochrome slag aggregates on the properties of alkali-activated blast furnace slag mortars. *Arabian Journal for Science and Engineering, 41*, 1561–1571. https://doi.org/10.1007/s13369-015-1910-8
Fares, A. I., Sohel, K., Al-Jabri, K., & Al-Mamun, A. (2021). Characteristics of ferrochrome slag aggregate and its uses as a green material in concrete–A review. *Construction and Building Materials, 294*, Article 123552. https://doi.org/10.1016/j.conbuildmat.2021.123552
Gallagher, L., & Peduzzi, P. (2019). Sand and sustainability: Finding new solutions for environmental governance of global sand resources. https://doi.org/10.13140/RG.2.2.33747.63526.
GB/T 14684-2011: Sand for Construction(in Chinese). (2011). *China Standard Press, Beijing*.
Güneyisi, E., Gesoğlu, M., Altan, İ, & Öz, H. Ö. (2015). Utilization of cold bonded fly ash lightweight fine aggregates as a partial substitution of natural fine aggregate in self-compacting mortars. *Construction and Building Materials, 74*, 9–16. https://doi.org/10.1016/j.conbuildmat.2014.10.021
Huynh, T.-P., Ho, L. S., & Van Ho, Q. (2022). Experimental investigation on the performance of concrete incorporating fine dune sand and ground granulated blast-furnace slag. *Construction and Building Materials, 347*, Article 128512. https://doi.org/10.1016/j.conbuildmat.2022.128512
Islam, M. Z., Sohel, K. M., Al-Jabri, K., & Al Harthy, A. (2021). Properties of concrete with ferrochrome slag as a fine aggregate at elevated temperatures. *Case Studies in Construction Materials, 15*, Article e00599. https://doi.org/10.1016/j.cscm.2021.e00599
JGJ70-2009: Standard for test method of performance on building mortar. (2009). *China Standard Press, Beijing*.
Jiang, Z. (2022). Production of Manufactured Sand. In (Ed.), *Green High-Performance Concrete with Manufactured Sand*. Springer. https://doi.org/10.1007/978-981-19-6313-1_2
Jiang, J., Feng, T., Chu, H., Wu, Y., Wang, F., Zhou, W., & Wang, Z. (2019). Quasi-static and dynamic mechanical properties of eco-friendly ultra-high-performance concrete containing aeolian sand. *Cement and Concrete Composites, 97*, 369–378. https://doi.org/10.1016/j.cemconcomp.2019.01.011
Kaufmann, J. (2020). Evaluation of the combination of desert sand and calcium sulfoaluminate cement for the production of concrete. *Construction and Building Materials, 243*, Article 118281. https://doi.org/10.1016/j.conbuildmat.2020.118281
Khan, M. I., Fares, G., Mourad, S., & Abbass, W. (2016). Optimized fresh and hardened properties of strain-hardening cementitious composites: Effect of sand size and workability. *Journal of Materials in Civil Engineering, 28*(12), 04016152. https://doi.org/10.1061/(ASCE)MT.1943-5533.0001665
Khattab, E. (2016). Effects of incorporating dune sand as fine aggregate replacement in self-compacting concrete. *Key Engineering Materials, 668*, 189–196. https://doi.org/10.4028/www.scientific.net/KEM.668.189
Koçyiğit, Ş. (2024). Performance evaluation of geopolymer mortars containing waste ferrochrome slag and fly ash for sustainable green building. *Scientific Reports, 14*(1), 14606. https://doi.org/10.1038/s41598-024-65552-w
Kong, D., Cai, J., Ren, J., Chen, Z., Shen, H., Yuan, J., & Qian, R. (2023). Influences of interlock-dense gradation designed by discrete element method on properties of cement-stabilized recycled brick-concrete aggregates. *Construction and Building Materials, 368*, Article 130494. https://doi.org/10.1016/j.conbuildmat.2023.130494
Kopuri, N., & Ramesh, K. (2019). Durability studies on concrete with ferro chrome slag as partial replacement of fine aggregate. *International Journal of Engineering Research and Technology, 8*, 159–164. https://doi.org/10.17577/IJERTV8IS030090
Kumar, C., Yaragal, S. C., & Das, B. (2020). Ferrochrome ash–Its usage potential in alkali activated slag mortars. *Journal of Cleaner Production, 257*, Article 120577. https://doi.org/10.1016/j.jclepro.2020.120577
Le, H. T., Kraus, M., Siewert, K., & Ludwig, H.-M. (2015). Effect of macro-mesoporous rice husk ash on rheological properties of mortar formulated from self-compacting high performance concrete. *Construction and Building Materials, 80*, 225–235. https://doi.org/10.1016/j.conbuildmat.2015.01.079
Li, H., Gao, P., Xu, F., Sun, T., Zhou, Y., Zhu, J., & Lin, J. (2021). Effect of fine aggregate particle characteristics on mechanical properties of fly ash-based geopolymer mortar. *Minerals, 11*(8), Article 897. https://doi.org/10.3390/min11080897
Li, Y., Zhang, H., Liu, G., Hu, D., & Ma, X. (2020). Multi-scale study on mechanical property and strength prediction of aeolian sand concrete. *Construction and Building Materials, 247*, Article 118538. https://doi.org/10.1016/j.conbuildmat.2020.118538
Liu, H., Chen, X., Che, J., Liu, N., & Zhang, M. (2020a). Mechanical performances of concrete produced with desert sand after elevated temperature. *International Journal of Concrete Structures and Materials, 14*, 1–15. https://doi.org/10.1186/s40069-020-00402-3
Liu, M., Liu, E., Hao, J. L., Di Sarno, L., & Xia, J. (2023). Hydration and material properties of blended cement with ground desert sand. *Construction and Building Materials, 389*, Article 131624. https://doi.org/10.1016/j.conbuildmat.2023.131624
Liu, Y., Li, Y., & Jiang, G. (2020b). Orthogonal experiment on performance of mortar made with dune sand. *Construction and Building Materials, 264*, Article 120254. https://doi.org/10.1016/j.conbuildmat.2020.120254
Luo, T., Yi, Y., Sun, Q., Li, L. G., Tang, L., & Hua, C. (2022). The effects of adding molybdenum tailings as cementitious paste replacement on the fluidity, mechanical properties and micro-structure of concrete. *Journal of Building Engineering, 62*, Article 105377. https://doi.org/10.1016/j.jobe.2022.105377
Ma, C., Zhao, B., Wang, L., Long, G., & Xie, Y. (2020). Clean and low-alkalinity one-part geopolymeric cement: Effects of sodium sulfate on microstructure and properties. *Journal of Cleaner Production, 252*, Article 119279. https://doi.org/10.1016/j.jclepro.2019.119279
Ma, G., Li, Z., & Wang, L. (2018). Printable properties of cementitious material containing copper tailings for extrusion based 3D printing. *Construction and Building Materials, 162*, 613–627. https://doi.org/10.1016/j.conbuildmat.2017.12.051
Manigandan, N., & Ponmalar, V. (2022). M5 investigation on ternary binder incorporated with ferrochrome slag aggregate in concrete. *Applied Nanoscience, 12*(12), 3925–3944.
Manigandan, N., & Ponmalar, V. (2024). M100 concrete probing on quinary cementitious matrix incorporated with industrial ferrochrome slag sand. *Construction and Building Materials, 420*, Article 135478. https://doi.org/10.1016/j.conbuildmat.2024.135478
Mithun B, Narasimhan M (2016) Performance of alkali activated slag concrete mixes incorporating copper slag as fineaggregate. Journal of Cleaner Production, 112, 837-844. https://doi.org/10.1016/j.jclepro.2015.06.026
Mishra, J., Nanda, B., Patro, S. K., Das, S. K., & Mustakim, S. M. (2022). Strength and microstructural characterization of ferrochrome ash-and ground

granulated blast furnace slag-based geopolymer concrete. *Journal of Sustainable Metallurgy*. https://doi.org/10.1007/s40831-021-00469-6
Moyo, L., Simate, G., & Mamvura, T. (2022). Magnesium recovery from ferrochrome slag: Kinetics and possible use in a circular economy. *Heliyon*. https://doi.org/10.1016/j.heliyon.2022.e12176
Nagarajan, M., & Vijayan, P. (2023). Some investigation on ternary powder (binder) technology incorporated with ferrochrome slag as fine aggregate in concrete. *Journal of Material Cycles and Waste Management, 25*(5), 2822–2834. https://doi.org/10.1007/s10163-023-01710-y
Nanda, A., Panda, S., & Panigrahi, S. K. (2025). Production of durable conventional concrete using recycled HDPE and PET plastic coarse aggregate. *Innovative Infrastructure Solutions, 10*(3), 1–17. https://doi.org/10.1007/s41062-025-01886-2
Neithalath, N., Sumanasooriya, M. S., & Deo, O. (2010). Characterizing pore volume, sizes, and connectivity in pervious concretes for permeability prediction. *Materials Characterization, 61*(8), 802–813. https://doi.org/10.1016/j.matchar.2010.05.004
Panda, C., Mishra, K., Panda, K., Nayak, B., & Nayak, B. (2013). Environmental and technical assessment of ferrochrome slag as concrete aggregate material. *Construction and Building Materials, 49*, 262–271. https://doi.org/10.1016/j.conbuildmat.2013.08.002
Panda, S., Pradhan, M., & Panigrahi, S. K. (2024a). Comparative study of OPC and PPC-based concrete properties containing bottom ash and fly ash as fine aggregate. *Indian Concrete Journal, 98*, 1–13.
Panda, S., Pradhan, M., & Panigrahi, S. K. (2024b). Optimal red mud replacement level evaluation in conventional concrete based on fresh and hardened concrete characteristics. *Journal of Sustainable Metallurgy, 10*(2), 835–850. https://doi.org/10.1007/s40831-024-00837-y
Peng, Y., Li, X., Liu, Y., Zhan, B., & Xu, G. (2020). Optimization for mix proportion of reactive powder concrete containing phosphorous slag by using packing model. *Journal of Advanced Concrete Technology, 18*(9), 481–492. https://doi.org/10.3151/jact.18.481
Rahul, A., Santhanam, M., Meena, H., & Ghani, Z. (2019). 3D printable concrete: Mixture design and test methods. *Cement and Concrete Composites, 97*, 13–23. https://doi.org/10.1016/j.cemconcomp.2018.12.014
Ren, C., Li, K., Wang, Y., Li, Y., Tong, J., & Cai, J. (2023). Preparation and hydration mechanisms of low carbon ferrochrome slag-granulated blast furnace slag composite cementitious materials. *Materials, 16*(6), 2385. https://doi.org/10.3390/ma16062385
Sanghamitra, B., & Reddy, C. (2017). Potential of ferro chrome slag as construction material. *Indian Highway, 45*(6), 11–17.
Santhosh, K. G., Subhani, S. M., & Bahurudeen, A. (2021). Cleaner production of concrete by using industrial by-products as fine aggregate: A sustainable solution to excessive river sand mining. *Journal of Building Engineering, 42*, Article 102415. https://doi.org/10.1016/j.jobe.2021.102415
Seif, E.-S.S.A. (2013). Assessing the engineering properties of concrete made with fine dune sands: An experimental study. *Arabian Journal of Geosciences, 6*, 857–863. https://doi.org/10.1007/s12517-011-0376-6
Sevim, Ö., & Demir, I. (2019). Physical and permeability properties of cementitious mortars having fly ash with optimized particle size distribution. *Cement and Concrete Composites, 96*, 266–273. https://doi.org/10.1016/j.cemconcomp.2018.11.017
Shafaei, D., Yang, S., Berlouis, L., & Minto, J. (2020). Multiscale pore structure analysis of nano titanium dioxide cement mortar composite. *Materials Today Communications, 22*, Article 100779. https://doi.org/10.1016/j.mtcomm.2019.100779
Shang, C., Wu, C., Lu, L., Yao, K., & Wang, J. (2022). Quantitative Assessment of the Sulphoaluminate Cement Embodied Carbon Emissions. In (Ed.), *ICCREM 2022*. https://doi.org/10.1061/9780784484562.018
Shi, J., Tan, J., Liu, B., Chen, J., Dai, J., & He, Z. (2021). Experimental study on full-volume slag alkali-activated mortars: Air-cooled blast furnace slag versus machine-made sand as fine aggregates. *Journal of Hazardous Materials, 403*, Article 123983. https://doi.org/10.1016/j.jhazmat.2020.123983
Shoukry, H., Perumal, P., Abadel, A., Alghamdi, H., Alamri, M., & Abdel-Gawwad, H. A. (2022). Performance of limestone-calcined clay cement mortar incorporating high volume ferrochrome waste slag aggregate. *Construction and Building Materials, 350*, Article 128928. https://doi.org/10.1016/j.conbuildmat.2022.128928
Song, Y., Dai, G., Zhou, J., Bian, Z., Zhao, L., & Song, L. (2020). Characterizing porous volume of cement-based concrete by multiscale image analysis. *Journal of Materials in Civil Engineering, 32*(9), 04020267. https://doi.org/10.1061/(ASCE)MT.1943-5533.0003355
Song, Y., Zhou, J.-W., Bian, Z.-N., & Dai, G.-Z. (2019). Pore structure characterization of hardened cement paste by multiple methods. *Advances in Materials Science and Engineering, 2019*, 1–18. https://doi.org/10.1155/2019/3726953
Tay, Y. W. D., Qian, Y., & Tan, M. J. (2019). Printability region for 3D concrete printing using slump and slump flow test. *Composites Part B, Engineering, 174*, Article 106968. https://doi.org/10.1016/j.compositesb.2019.106968
Team, P. Chromium—a National Mineral Commodity Perspective, Open File Report 2007-1167. *USGS-US. Geological Survey*. https://doi.org/10.3133/ofr20071167
Xia, D., Chen, R., Cheng, J., Tang, Y., Xiao, C., & Li, Z. (2023). Desert sand-high calcium fly ash-based alkali-activated mortar: Flowability, mechanical properties, and microscopic analysis. *Construction and Building Materials, 398*, Article 131729. https://doi.org/10.1016/j.conbuildmat.2023.131729
Xiao, J., Qiang, C., Nanni, A., & Zhang, K. (2017). Use of sea-sand and seawater in concrete construction: Current status and future opportunities. *Construction and Building Materials, 155*, 1101–1111. https://doi.org/10.1016/j.conbuildmat.2017.08.130
Yaragal, S. C., Kumar, B. C., & Jitin, C. (2020). Durability studies on ferrochrome slag as coarse aggregate in sustainable alkali activated slag/fly ash based concretes. *Sustainable Materials and Technologies, 23*, Article e00137. https://doi.org/10.1016/j.susmat.2019.e00137
Zelić, J. (2005). Properties of concrete pavements prepared with ferrochromium slag as concrete aggregate. *Cement and Concrete Research, 35*(12), 2340–2349. https://doi.org/10.1016/j.cemconres.2004.11.019
Zhang, C., Hou, Z., Chen, C., Zhang, Y., Mechtcherine, V., & Sun, Z. (2019a). Design of 3D printable concrete based on the relationship between flowability of cement paste and optimum aggregate content. *Cement and Concrete Composites, 104*, Article 103406. https://doi.org/10.1016/j.cemconcomp.2019.103406
Zhang, M., Liu, H., Sun, S., Chen, X., & Doh, S. I. (2019b). Dynamic mechanical behaviors of desert sand concrete (DSC) after different temperatures. *Applied Sciences, 9*(19), 4151. https://doi.org/10.3390/app9194151
Zhang, M., Zhu, X., Shi, J., Liu, B., He, Z., & Liang, C. (2022). Utilization of desert sand in the production of sustainable cement-based materials: A critical review. *Construction and Building Materials, 327*, Article 127014. https://doi.org/10.1016/j.conbuildmat.2022.127014
Zhu, Y., Rong, Z., Jiao, M., Jiang, Q., & Wu, J. (2023). Valorization and enhancement mechanism of ferrochrome slag as aggregate for manufacturing ultra-high performance concrete (UHPC). *Cement and Concrete Composites, 144*, Article 105298. https://doi.org/10.1016/j.cemconcomp.2023.105298

Publisher's Note

Hailong Wang Professor, School of Civil Engineering and Architecture, Zhejiang University. Research focus: Concrete structural mechanics, corrosion-resistant structures.

Junyi Shen PhD Candidate, School of Civil Engineering and Architecture, Zhejiang University. Research focus: Concrete bridge structures, intelligent construction technologies.

Qamar Shahzad PhD Candidate, College of Civil Engineering, Tongji University. Research focus: Intelligent construction technologies.

Xiaoyan Sun Professor , School of Civil Engineering and Architecture, Zhejiang University. Research focus: Degradation mechanisms of bridge concrete, life-cycle performance assessment. Email: selina@zju.edu.cn

Weiwei Dong Professor, Centre for Balance Architecture, Zhejiang University. Research focus: Concrete structural mechanics.